

Regulating the distribution of iron active sites on γ -Fe₂O₃ via Mn-modified α -Fe₂O₃ for NH₃-SCR

Donghai Mo ^{a,b,c}, Qiuju Qin ^{a,b,c}, Chengheng Huang ^{a,b,c}, Lin Tao ^{a,b,c}, Chen Li ^{a,b,c}, Jiaqi Qiu ^{a,b,c}, Jingkai Wang ^{a,b,c}, Xiaorong Han ^{a,b,c}, Shifei Gu ^{a,b,c}, Zhengjun Chen ^{a,b,c}, Bin Li ^{a,b,c}, Lihui Dong ^{a,b,c,*}

^a State Key Laboratory of Featured Metal Materials and Life-cycle Safety for Composite Structures, Guangxi University, Nanning 530004, PR China

^b Guangxi Key Laboratory of Petrochemical Resource Processing and Process Intensification Technology, School of Chemistry and Chemical Engineering, Guangxi University, Nanning 530004, PR China

^c Guangxi Colleges and Universities Key Laboratory of Applied Chemistry Technology and Resource Development, School of Chemistry and Chemical Engineering, Guangxi University, Nanning 530004, PR China



ARTICLE INFO

Keywords:

NH₃-SCR

Low temperature

Fe₂O₃

Magnetism

Crystal-active sites relationship

ABSTRACT

Developing below 150 °C highly activity and broad reaction window catalysts has been challenging by using Fe-based catalysts for NH₃-SCR. The octahedral Fe³⁺ (Fe_{Oh}³⁺) sites exist in hematite (α -Fe₂O₃) and maghemite (γ -Fe₂O₃) are inactive for NH₃-SCR due to the redox circle of Fe²⁺→Fe³⁺ reliance on the distribution of iron sites in crystal structure. Here we modified the α -Fe₂O₃ crystal structure by substituting part inactive Fe_{Oh}³⁺ sites with catalytically active Mn_{Oh}³⁺ sites, which promoted the formation of γ -Fe₂O₃ to generate the active tetrahedral Fe³⁺ (Fe_{Td}³⁺) sites and enhanced the magnetism of the Fe_{1-y}Mn_yO_x. The strong Fe-O-Mn interaction established by crystal coordinative configurations not only boosted the formation of NO₂ but also facilitated the Brønsted acid circle. Surprisingly, the Fe_{0.85}Mn_{0.15}O_x exhibited the superior low temperature NH₃-SCR activity, with NO_x conversion above 100% at 100–275 °C under a GHSV of 60000 h⁻¹.

1. Introduction

Nitrogen oxides that containing NO and NO₂ mainly emitted by power stations, factories and automobiles have made great contributions to air pollution, significantly affecting global tropospheric chemistry and seriously endangering human health [1,2]. At present, it is considered to be an efficient and practical method to use vanadium metal oxide as catalyst to achieve efficient NO elimination in NH₃-SCR technology. Developing environmental-friendly and low-temperature (LT) high-efficiency catalysts is necessary due to the poor catalytic activity below 150 °C and secondary pollution caused by serious bio-toxicity hinder the scope of applications of vanadium-based catalysts [3].

Iron-based catalysts have attracted much attention from researchers because of environment-friendly, low economic cost and catalytic stability in the middle and high temperature window for NH₃-SCR. Among the crystalline phases of Fe₂O₃, maghemite (γ -Fe₂O₃) and hematite

(α -Fe₂O₃) are the most widely investigated for NH₃-SCR [4,5]. Hematite (α -Fe₂O₃) has a rhombohedral centered hexagonal structure consisting only of Fe_{Oh}³⁺ sites in which Fe³⁺ ions occupying the octahedral oxygen center, maghemite (γ -Fe₂O₃) has a spinel structure centered on tetrahedral Fe³⁺ (Fe_{Td}³⁺) and octahedral Fe³⁺ (Fe_{Oh}³⁺) sites [6]. Qu et al. creatively demonstrated that Fe_{Td}³⁺ sites as the catalytically active sites (CASs) in NH₃-SCR by substituting the Fe_{Td}³⁺ sites and Fe_{Oh}³⁺ sites with inactive Ti⁴⁺ or Zn²⁺ respectively and found the electron transfer between Fe³⁺ and Fe²⁺ is promoted in Fe_{Td}³⁺ sites compared with Fe_{Oh}³⁺ sites [7]. Liu et al. found the α -Fe₂O₃ catalysts exhibited lower catalytic performance than γ -Fe₂O₃ below 200 °C due to stable nitrates more easily formed on α -Fe₂O₃ surface than γ -Fe₂O₃ and blocked the active sites [8]. Wen et al. prepared FeNb_{0.4}O_x-C catalyst by coprecipitation with the assistance of CTAB to induce generate γ -Fe₂O₃. The interaction between Fe-Nb and brought about more active sites hence enhanced the NO_x conversion [9]. Despite many achievements have been made in the study of iron oxides in NH₃-SCR, developing the wide operating temperature window and

* Corresponding author at: State Key Laboratory of Featured Metal Materials and Life-cycle Safety for Composite Structures, Guangxi University, Nanning 530004, PR China.

E-mail address: donglh@gxu.edu.cn (L. Dong).

the excellent LT activity (below ~ 150 °C) remains a crucial bottleneck for Fe_2O_3 -based catalysts. The performance of representative of iron-based catalysts for NH_3 -SCR in recent five years is summarized in Table 1.

Manganese oxides with variable valence states and excellent redox ability are commonly investigated for NH_3 -SCR. Although manganese-based materials showing an excellent LT SCR activity, restraining their practical applications because of sensitivity to SO_2 , poor N_2 selectivity and show narrow working temperature window [10,11]. However, manganese oxides as additives for other metal oxides can enhance the redox ability and increase Brønsted acid sites on NH_3 -SCR catalysts [12]. The flexible valence states of manganese oxides facilitate the electronic transfer with other metal ions and formation of abundant active oxygen, thus promoting the NO oxidize to NO_2 and trigger the “Fast SCR” reaction at low temperatures [13,14]. Zhang et al. found that Mn doping can optimize the structure of $\gamma\text{-Fe}_2\text{O}_3$ and form Fe-Mn solid solution, thus improving the SCR activity at low temperature [49]. Lai et al. report on a Fe-Mn system, the existence of manganese causes the lattice contraction of $\gamma\text{-Fe}_2\text{O}_3$ and increases the activation energy of construct $\alpha\text{-Fe}_2\text{O}_3$, thus maintaining the crystal phase of $\gamma\text{-Fe}_2\text{O}_3$ at high temperature [15].

Transformation of crystal phase structure and CASs are essential in NH_3 -SCR for iron-based oxides due to the formation of $\alpha\text{-Fe}_2\text{O}_3$ above 320 °C. Relationship between crystal structure and CASs of Fe_2O_3 is crucial for elaborate any catalytic reaction mechanism and for the logical devise of high- efficient and low-temperature NH_3 -SCR catalysts. However, the distribution of the doping element and transformation of crystal phase leads to the change of CASs in crystal structure of Fe_2O_3 are seldom investigated on NH_3 -SCR. In this work, to induce the transition from $\alpha\text{-Fe}_2\text{O}_3$ to $\gamma\text{-Fe}_2\text{O}_3$ structure and generate more active Fe^{3+} CASs of the iron oxide catalyst, we have modified the Fe_2O_3 crystal structure by substituting part inactive $\text{Fe}_{\text{O}h}^{3+}$ sites with catalytically active $\text{Mn}_{\text{O}h}^{3+}$ sites. Herein, a series of $\text{Fe}_{1-y}\text{Mn}_y\text{O}_x$ was prepared by sol-gel strategy, compared with pure Fe_2O_3 , the $\text{Fe}_{0.85}\text{Mn}_{0.15}\text{O}_x$ catalyst exhibited the superior LT catalytic performance and extensive reaction window.

2. Experimental section

2.1. Catalyst preparation

The $\alpha\text{-Fe}_2\text{O}_3$, $\gamma\text{-Fe}_2\text{O}_3$, $\gamma\text{-Mn}_2\text{O}_3$ and $\text{Fe}_{1-y}\text{Mn}_y\text{O}_x$ series catalysts were acquired by sol-gel strategy. First, a 10 ml mixed solution containing 4.04 g of $\text{Fe}(\text{NO}_3)_3 \cdot 9\text{H}_2\text{O}$ and a specified amount of Mn (CH_3COO)₂·4H₂O (The molar ratio of Mn/Fe atoms is contained within range 0–20%) was prepared with deionized water. Second, the mixed solution is then added drop by drop to the 10 ml deionized aqueous solution of citric acid monohydrate (0.73 g/ml). Third, the precursor solution was continuously mixed for 0.5 h, then 30 mg polyethylene glycol (PEG 2000) was added and transferred to a magnetic stirring oil bath at 80 °C for 4 h to obtain a stable gel. Next, the gel was dried at 100 °C for 12 h. Lastly, the catalyst was obtained by grinding the dried material into powder and calcining it at 350 °C in air for 4 h. $\gamma\text{-Fe}_2\text{O}_3$ acquired by calcined at 250 °C for 2 h. The catalyst is named after the proportion of doped manganese in the total amount of metal atoms. For instance, the $\text{Fe}_{0.85}\text{Mn}_{0.15}\text{O}_x$ catalyst contains 15% of Mn in the total amount of metal atoms.

2.2. Catalysts characterization

X-ray diffraction (XRD) data of the catalysts were collected on a Bruker D8 with Cu K α radiation at 40 kV and 30 mA and the scanning range was set at 20 of 10–80 ° with a scanning speed of 10 °/min.

The morphology and microstructure of the samples were observed by field emission scanning electron microscopy (SEM) at 20 kV (FEI Quattro S, Czech).

The energy-dispersive X-ray spectroscopy (EDS) images were

Table 1
Representative of iron-based catalysts for the NH_3 -SCR in recent five years.

catalysts	preparation method	reaction condition	NO conversion	ref
Fe-Ce	sol-gel	$\text{NO} = \text{NH}_3 = 500 \text{ ppm, 5 vol\%}$ $\text{O}_2, \text{GHSV} = 90000 \text{ h}^{-1}$	~100%, (200–300 °C)	[4]
Fe-Nb	co-precipitation	$\text{NO} = \text{NH}_3 = 500 \text{ ppm, 5 vol\%}$ $\text{O}_2, \text{GHSV} = 250000 \text{ h}^{-1}$	> 90%, (250–400 °C)	[9]
Fe-Ce-S	co-precipitation	$\text{NO} = \text{NH}_3 = 500 \text{ ppm, 5 vol\%}$ $\text{O}_2, \text{GHSV} = 100000 \text{ h}^{-1}$	~100%, (225–350 °C)	[16]
Fe-V-Ti	co-precipitation	$\text{NO} = \text{NH}_3 = 500 \text{ ppm, 5 vol\%}$ $\text{O}_2, \text{GHSV} = 200000 \text{ h}^{-1}$	~100%, (225–375 °C)	[17]
FeMnTiO _x -tourmaline	sol-gel	$\text{NO} = \text{NH}_3 = 800 \text{ ppm, 5 vol\%}$ $\text{O}_2, \text{GHSV} = 50000 \text{ h}^{-1}$	> 80%, (160–380 °C)	[18]
$\text{SO}_4^{2-}/\alpha\text{-Fe}_2\text{O}_3$	impregnation	$\text{NO} = \text{NH}_3 = 600 \text{ ppm, 5 vol\%}$ $\text{O}_2, \text{GHSV} = 60000 \text{ h}^{-1}$	~100%, (275–400 °C)	[19]
FeVO ₄ /CeO ₂	sol-gel	$\text{NO} = \text{NH}_3 = 500 \text{ ppm, 5 vol\%}$ $\text{O}_2, \text{GHSV} = 80000 \text{ h}^{-1}$	> 90%, (225–350 °C)	[20]
Fe-Mn-Mo/TiO ₂	impregnation	$\text{NO} = \text{NH}_3 = 400 \text{ ppm, 3 vol\%}$ $\text{O}_2, \text{GHSV} = 30000 \text{ h}^{-1}$	~100%, (250–300 °C)	[21]
Fe-Cu	urea-assisted	$\text{NO} = \text{NH}_3 = 500 \text{ ppm, 3 vol\%}$ $\text{O}_2, \text{GHSV} = 60000 \text{ h}^{-1}$	> 90%, (150–275 °C)	[50]
$\text{Fe}_2\text{O}_3\text{SO}_4^{2-}/(\text{TiO}_2\text{-ZrO}_2)$	impregnation	$\text{NO} = \text{NH}_3 = 500 \text{ ppm, 3 vol\%}$ $\text{O}_2, \text{GHSV} = 47000 \text{ h}^{-1}$	~100%, (300–500 °C)	[51]
Ti-Fe ₂ O ₃	co-precipitation	$\text{NO} = \text{NH}_3 = 600 \text{ ppm, 3 vol\%}$ $\text{O}_2, \text{GHSV} = 72000 \text{ h}^{-1}$	> 90%, (210–350 °C)	[52]
CeO ₂ -Fe ₂ O ₃ -MoO ₃	impregnation	$\text{NO} = \text{NH}_3 = 500 \text{ ppm, 5 vol\%}$ $\text{O}_2, \text{GHSV} = 75000 \text{ h}^{-1}$	> 90%, (225–350 °C)	[53]
TiO ₂ @Fe ₂ O ₃ @Al ₂ O ₃	impregnation	$\text{NO} = \text{NH}_3 = 500 \text{ ppm, 5 vol\%}$ $\text{O}_2, \text{GHSV} = 20000 \text{ h}^{-1}$	> 90%, (220–420 °C)	[54]
MnFe-TOS	hydrothermal	$\text{NO} = \text{NH}_3 = 500 \text{ ppm, 5 vol\%}$ $\text{O}_2, \text{GHSV} = 30000 \text{ h}^{-1}$	> 80%, (180–380 °C)	[55]
Zr/Fe-SSZ-13	hydrothermal	$\text{NO} = 1000 \text{ ppm, NH}_3 = 1100 \text{ ppm, 5 vol\% O}_2, \text{GHSV} = 30000 \text{ h}^{-1}$	> 90%, (350–575 °C)	[56]
Fe-CePO ₄	co-precipitation	$\text{NO} = \text{NH}_3 = 500 \text{ ppm, 5 vol\%}$ $\text{O}_2, \text{GHSV} = 60000 \text{ h}^{-1}$	~100%, (240–380 °C)	[57]
Fe-Nb-Ti	sol-gel	$\text{NO} = \text{NH}_3 = 500 \text{ ppm, 4 vol\%}$ $\text{O}_2, \text{GHSV} = 24000 \text{ h}^{-1}$	> 80%, (~200 °C)	[58]
Fe-OMS-2	hydrothermal	$\text{NO} = \text{NH}_3 = 500 \text{ ppm, 5 vol\%}$ $\text{O}_2, 8 \text{ vol\% H}_2\text{O, GHSV} = 40000 \text{ h}^{-1}$	> 90%, (125–300 °C)	[59]

(continued on next page)

Table 1 (continued)

catalysts	preparation method	reaction condition	NO conversion	ref
WO ₃ -FeO _x	solvent-free	NO = NH ₃ = 600 ppm, 5 vol% O ₂ , GHSV = 60000 h ⁻¹	~100%, (250–450 °C)	[60]

obtained by the Tecnai G2 F20 S-TWIN instrument of FEI Company, the highresolution transmission electron microscope (HRTEM) images were acquired under an accelerating voltage of 200 kV. Test preparation: ultrasonic the sample in ethanol solution for 10 min, then drop the sample solution into the copper mesh for testing.

The N₂ adsorption-desorption curve was tested on Micrometric Stristari3020 at a temperature of 77 K and the samples were pretreated at 300 °C for 4 h. The pore size distribution and specific surface area of the catalyst were calculated using the Barrett-Joyner-Halenda (BJH) method and the Brunauer-Emmet-Teller (BET) equation.

In situ DRIFTS data were collected in Nicolet IS50 FT-IR spectrometer with a resolution of 4 cm⁻¹ and a scan count of 32. A certain amount of the catalyst was filled in the reaction cell and pretreated for 0.5 h N₂ purging at 110 °C (pretreatment temperature at 300 °C for NH₃ adsorption-desorption) and the background image is obtained at 50–300 °C (50 °C each step) during the sample cooling process. The sample spectrum was collected within 50–300 °C after the pre-adsorption of the reaction gas for 1 h. Test conditions: NO = NH₃ = 500 ppm, O₂ = 5 vol%, balance N₂ and GHSV = 60,000 h⁻¹.

H₂-TPR and O₂/NH₃-TPD experiments were performed using a FINESORB-3010 automatic chemical adsorption instrument. All samples used for testing are 40–60 mesh in size and the gas flow rate used is 10 ml/min. For H₂-TPR, 25 mg samples were pretreated at 110 °C in N₂ atmosphere for 1 h. The H₂-Ar mixture (7 vol% H₂, Ar as the equilibrium gas) was introduced as reducing gas pre-adsorption for 30 min after samples cooled to room temperature. For O₂-TPD or NH₃-TPD, 50 mg samples were pretreated at 200 °C or 300 °C for 1 h in He stream. The O₂ (pure O₂) or NH₃ (5 vol% NH₃, N₂ as the equilibrium gas) was introduced as adsorption gas pre-adsorption for 1 h after samples cooled to room temperature and then purging in the He atmosphere for 30 min. Finally, the samples were raised from room temperature to 800 °C at a heating rate of 10 °C/min, and the data of H₂-TPR, O₂-TPD and NH₃-TPD was collected by thermal conductivity detector (TCD).

X-ray photoelectron spectroscopy (XPS) were carried out on Thermo Fisher Scientific ESCALAB 250XI and the data were corrected based on C 1 s = 284.8 eV.

The hysteresis loop of the catalyst was obtained by vibrating sample magnetometer (VSM) Lake Shore 7404 and the moment measuring range: 5×10⁻⁷–10³ emu.

2.3. Catalytic performance evaluation

The NO, NO₂ and N₂O concentration in catalytic reaction was determined by FGA10 flue gas analyzer. A Nicolet IS50 FT-IR spectrometer was used to detect the concentrations of NH₃. All tests used 40–60 mesh 100 mg samples with a 10 mm O.D. quartz tube. Water vapor in flue gas is produced by FD-WG water vapor generator (Furende Inc). The concentration and composition of reaction gas standard cylinders used are as follows: NO (1250 ppm NO, N₂ as the equilibrium gas), NH₃ (1271 ppm NH₃, N₂ as the equilibrium gas), O₂ (15% O₂, N₂ as the equilibrium gas), SO₂ (1027 ppm SO₂, N₂ as the equilibrium gas). In the reaction process, the flow rate is controlled by using type MT-50–2 J flowmeters to generate defined concentrations.

Reaction conditions: NO = NH₃ = 500 ppm, O₂ = 5 vol%, SO₂ = 25 ppm (when used), H₂O = 5 vol% (when used). The NO conversion and N₂ selectivity 50–300 °C was calculated as followed

$$\text{NO conversion} = \left[\frac{[\text{NO}]_{\text{in}} - [\text{NO}]_{\text{out}}}{[\text{NO}]_{\text{in}}} \right] \times 100\%$$

$$\text{N}_2 \text{ selectivity} = \left[1 - \frac{2[\text{N}_2\text{O}]_{\text{out}} + [\text{NO}_2]_{\text{out}}}{[\text{NO}]_{\text{in}} - [\text{NO}]_{\text{out}} + [\text{NH}_3]_{\text{in}} - [\text{NH}_3]_{\text{out}}} \right] \times 100\%$$

3. Results and discussion

3.1. NH₃-SCR performance and H₂O/SO₂ tolerance

In order to study that influence of manganese doping into Fe₂O₃ on catalytic performance. The low-temperature SCR performance over catalysts were test in the range of 50–300 °C, 25 °C for each step. The results of NO conversion are shown in Fig. 1(a), it can be seen that the highest NO conversion of α -Fe₂O₃ catalyst only achieve 65% in the 275 °C and inactivity at 50–150 °C. In comparison, the pure γ -Fe₂O₃ shows ~90% NO conversion at 250–300 °C and γ -Mn₂O₃ shows ~80% NO conversion at 150–250 °C. However, after the modified the Fe₂O₃ crystal structure by doping manganese, the NO conversion of the catalysts is improved significantly. It is worth noting that among Fe₂O₃ and all Fe_{1-y}Mn_yO_x catalysts, Fe_{0.85}Mn_{0.15}O_x exhibits the best NH₃-SCR performance which achieves above 85% in the 75 °C and nearly 100% within 100–275 °C at a GHSV of 60,000 h⁻¹. Moreover, the activity of Fe_{1-y}Mn_yO_x catalysts is enhance with the manganese content increase from 5% to 20% at low temperatures (50–150 °C) while decrease the activity when the manganese content over 15% at high temperatures (over 200 °C). This means that the introduction of manganese produces more catalytically active sites (CASs) in Fe_{1-y}Mn_yO_x catalysts for NH₃-SCR. It was noted that the activity of the Fe_{0.80}Mn_{0.20}O_x began to decline at 200 °C, which was mainly caused by the adsorption of NH₃ on acidic sites is weakened and the occurrence of side reaction of NH₃ over-oxidation at high temperatures results in less reductant [22,23]. Thus, the balance in redox circle and acid circle is crucial for Fe_{0.85}Mn_{0.15}O_x have the capability to exhibit the superior LT NH₃-SCR activity and a broad reaction window. The N₂ selectivity of the catalysts for the NH₃-SCR reaction were calculated and shown in Fig. 1(b). It can be seen that γ -Fe₂O₃ shows better N₂ selectivity than α -Fe₂O₃ and γ -Mn₂O₃ in the whole temperature window and nearly 100%. Notably, compared with pure Fe₂O₃, the introduction of Mn caused the production of N₂O as a by-product at 125 °C (Fig S1), which led to the decrease of the N₂ selectivity of the Fe_{1-y}Mn_yO_x. In addition, the stability of the Fe_{0.85}Mn_{0.15}O_x catalyst was tested and shown in Fig. S2. The Fe_{0.85}Mn_{0.15}O_x catalyst can maintain nearly 100% NO conversion and 90% N₂ selectivity at 150 °C for 24 h. The H₂O and SO₂ resistance over α -Fe₂O₃ and Fe_{0.85}Mn_{0.15}O_x were investigated due to H₂O and SO₂ are inevitably exist in actual flue gas. As depicted in the Fig. 1(c) and (d). When 5 vol% H₂O was turned on the reaction gas at 250 °C, α -Fe₂O₃ and Fe_{0.85}Mn_{0.15}O_x catalysts is no obvious fluctuation in 3 h of the NO conversion, however, when we increase the water vapor content from 5 to 10 vol%, it can be seen in the Fig. 1(d), NO conversion of α -Fe₂O₃ decreases from 63% to 47%, while the NO conversion of Fe_{0.85}Mn_{0.15}O_x can still maintain nearly 100%, showing that the excellent water-resistant ability of Fe_{0.85}Mn_{0.15}O_x after Mn modified the Fe₂O₃ crystal structure. In addition, the NO conversion of α -Fe₂O₃ decreased from 60% to 23% in 3 h when 25 ppm SO₂ was turned on the reaction gas at 250 °C while Fe_{0.85}Mn_{0.15}O_x was maintained at ~90% was observed after being tested. This means that the sulfur resistance has been improved by modified the Fe₂O₃ crystal. Besides, the NO conversion of Fe_{0.85}Mn_{0.15}O_x still decrease after turn off 5 vol% H₂O and irreversible after being poisoned by SO₂, which means SO₂ is the main reason cause Fe_{0.85}Mn_{0.15}O_x inactivation.

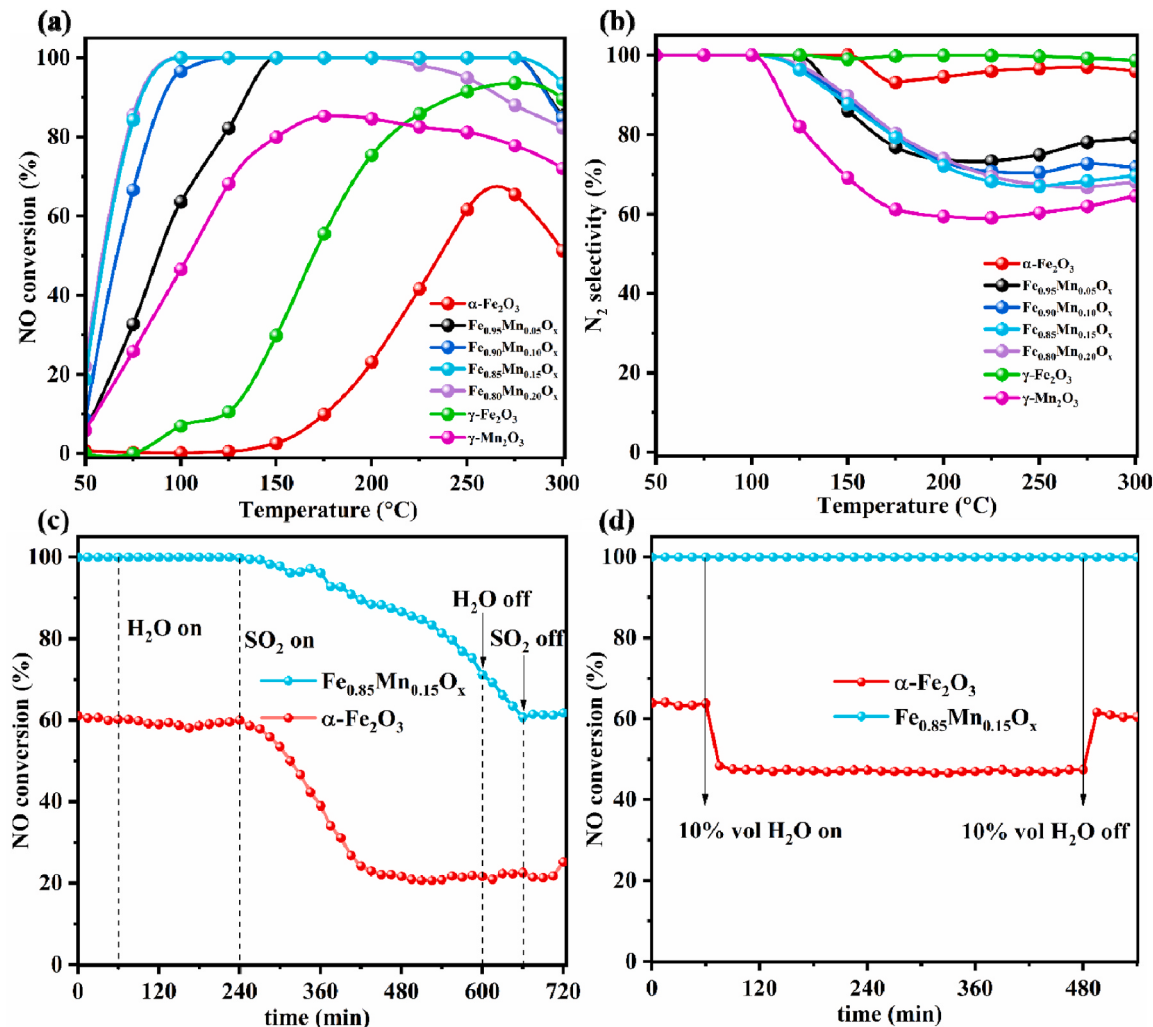


Fig. 1. NH₃-SCR performance of catalysts: (a) NO conversion of catalysts; (b) N₂ selectivity of the catalysts for the NH₃-SCR reaction; (c) The 5 vol% H₂O and SO₂ tolerance of Fe_{0.85}Mn_{0.15}O_x and α-Fe₂O₃ at 250 °C; (d) The 10 vol% H₂O tolerance of Fe_{0.85}Mn_{0.15}O_x and α-Fe₂O₃ at 250 °C. Reaction conditions: NO = NH₃ = 500 ppm, O₂ = 5 vol%, H₂O = 5 or 10 vol% (when used), SO₂ = 25 ppm (when used), balance N₂ and GHSV = 60,000 h⁻¹.

3.2. Structure and morphology

3.2.1. XRD analysis

To obtain structural information on the Mn modified the Fe₂O₃ catalysts. Fig. 2(a) show the XRD spectrum of the Fe_{1-y}Mn_yO_x catalysts with various manganese-doped contents and pure Fe₂O₃. Pure Fe₂O₃ is identified as hematite (α-Fe₂O₃) with a hexagonal structure (JPCDS Card No. 33-0664) [8,24]. Additionally, there are some new diffraction peaks appeared after doping manganese, while no diffraction peak belongs to MnO_x can be detected. This distinct shows that Mn doped into the Fe₂O₃ crystal lattice [25]. The diffraction peaks at 30.3°, 35.7°, 37.4°, 43.5°, 53.9°, 57.5° and 63.1° can be well indexed to γ-Fe₂O₃ (JCPDS Card No. 39-1346), corresponding to the lattice planes of (2 2 0), (3 1 1), (2 2 2), (4 0 0), (4 2 2), (5 1 1) and (4 4 0) [7,8,15]. With increasing manganese content is increased from 5% to 20%, all the intensity of diffraction peaks of the α-Fe₂O₃ becoming weaken and the γ-Fe₂O₃ gradually increases. This means that the crystalline phase can be induced from α-Fe₂O₃ to γ-Fe₂O₃ by introducing manganese. Note that all the peaks of Fe_{1-y}Mn_yO_x clearly shift to larger Bragg angles in comparison to γ-Fe₂O₃. This occurs after substitution of part Fe_{OH}³⁺ with Mn³⁺ in α-Fe₂O₃ and generate Fe_{Td}³⁺ of γ-Fe₂O₃, which brought about lattice contraction [15]. Furthermore, we calculate the crystallite sizes, lattice constants of (2 2 0) peaks and to quantify the ratio of α/γ Fe₂O₃ of the Fe_{1-y}Mn_yO_x catalysts and the results comparison with pure γ-Fe₂O₃ are summarized

in Table 2. In consideration of ionic radius of Fe_{Td}³⁺ (0.49 Å) and Fe_{OH}³⁺ (0.65 Å), the Mn³⁺ (0.58 Å) is smaller than that of Fe_{OH}³⁺ (0.65 Å) [7], the related changes in the lattice parameters calculated from the (2 0 0) peaks indicating that substitution of part Fe_{OH}³⁺ with Mn³⁺ in Fe_{1-y}Mn_yO_x after Mn modified. This conclusion is consistent with XPS analysis and support by H₂-TPR results.

3.2.2. VSM analysis

To further study the impact of formation γ-Fe₂O₃ and the influence of the magnetic properties, the α-Fe₂O₃, γ-Fe₂O₃ and Fe_{1-y}Mn_yO_x catalysts were measured by vibrating sample magnetometer (VSM). The M-H curves of α-Fe₂O₃, γ-Fe₂O₃ and Fe_{1-y}Mn_yO_x are shown in Fig. 2(c) and summary of the magnetic properties are shown in Table 3. It is found that the introduction of Mn can enhance the coercivity (M_r) and saturation magnetization (M_s) of Fe_{1-y}Mn_yO_x remarkably. When the doping content of manganese is increased to 15%, the value of M_r and M_s reached the maximum value 46.16 emu/g and 5.91 emu/g, respectively. In comparison with γ-Fe₂O₃ that M_r and M_s value is 42.05 emu/g and 0.94 emu/g, respectively, Fe_{0.85}Mn_{0.15}O_x shows better magnetism. It has been reported that the increase of magnetism can improve the adsorption of NO at low temperature on the catalyst surface because NO is a paramagnetic molecule and degaussing of catalyst at high temperature [15,24,25]. Furthermore, the increased magnetization of Fe_{1-y}Mn_yO_x is positively related to the promotion of γ-Fe₂O₃ formation

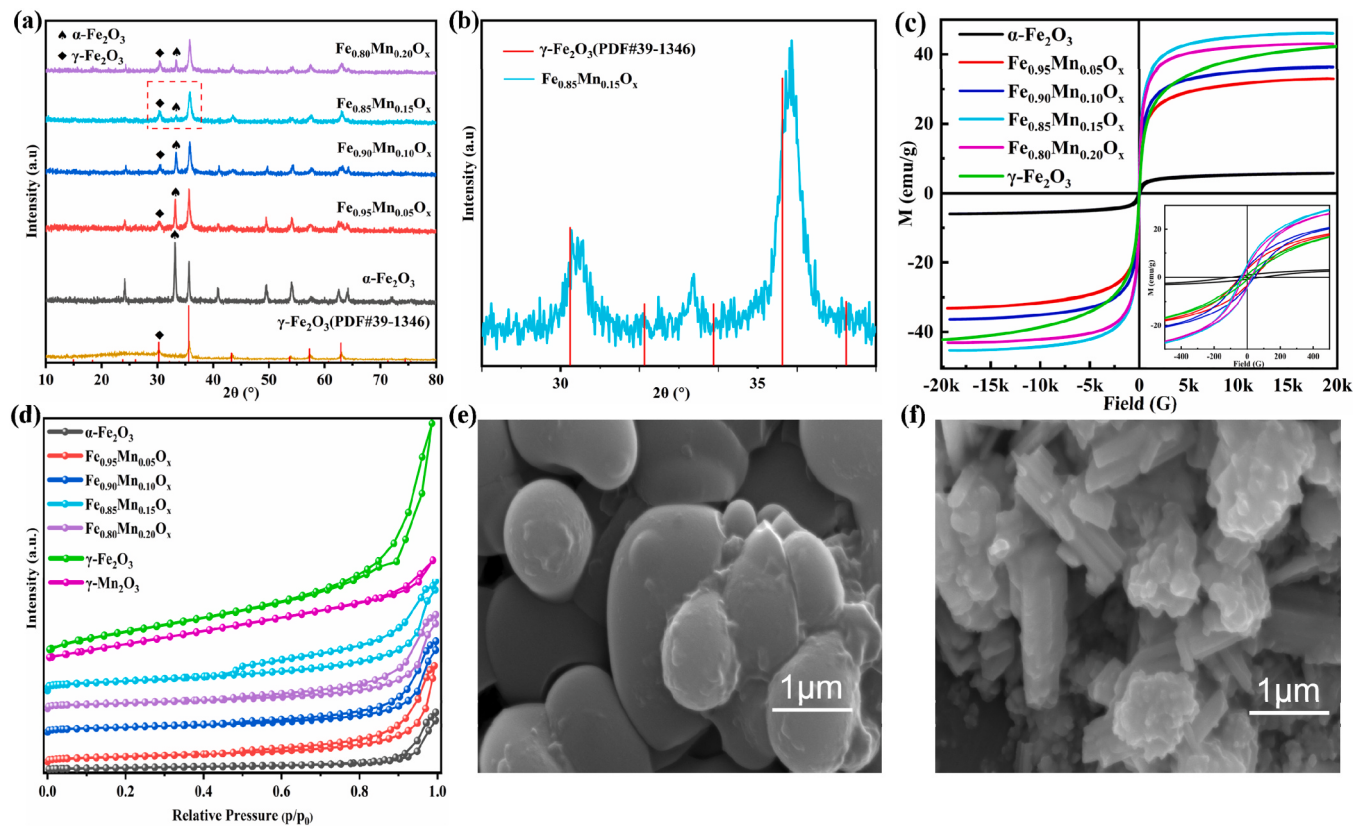


Fig. 2. (a) XRD spectra of the catalysts; (b) the partial enlarged detail of Fe_{0.85}Mn_{0.15}O_x and γ-Fe₂O₃ (PDF#39-1346); (c) Samples' room-temperature magnetization curves of the catalysts; (d) N₂ adsorption-desorption isotherms of the catalysts; SEM images of (e) α-Fe₂O₃ and (f) Fe_{0.85}Mn_{0.15}O_x.

Table 2
Summary of the XRD data analysis of the Fe_{1-y}Mn_yO_x catalysts and γ-Fe₂O₃.

Samples	crystallite sizes (Å)	lattice constants (Å)	γ/ (α+γ) Fe ₂ O ₃ (%)
Fe _{0.95} Mn _{0.05} O _x	116	8.34	61.0
Fe _{0.90} Mn _{0.10} O _x	132	8.32	63.3
Fe _{0.85} Mn _{0.15} O _x	132	8.30	75.8
Fe _{0.80} Mn _{0.20} O _x	127	8.31	73.0
γ-Fe ₂ O ₃	103	8.36	100

Table 3
Summary of the magnetic properties of the samples.

Samples	M _s (emu/g)	M _r (emu/g)	H _c (Oe)
α-Fe ₂ O ₃	5.78	0.87	92.44
Fe _{0.95} Mn _{0.05} O _x	33.96	3.14	46.10
Fe _{0.90} Mn _{0.10} O _x	36.34	3.90	46.21
Fe _{0.85} Mn _{0.15} O _x	46.16	5.91	35.37
Fe _{0.80} Mn _{0.20} O _x	43.05	4.29	31.45
γ-Fe ₂ O ₃	42.05	0.94	14.89

in XRD results and Fe_{0.85}Mn_{0.15}O_x show the best catalytic activity, which may be due to the difference of NO adsorption on the surface caused by the magnetism of the catalyst. These factors will be discussed in the in-situ DRIFT results.

3.2.3. BET analysis

The specific surface area is an important factor affecting the adsorption capacity of reaction gas on the catalyst. As depicted in Fig. 2 (d) and Fig. S3, the isotherms of the α-Fe₂O₃, γ-Fe₂O₃, γ-Mn₂O₃ and Fe_{1-y}Mn_yO_x catalysts exhibit typical IV curves at high relative pressure and the pore sizes are corresponding to mesoporous material (2–50 nm)

[26,27]. Table 4 summarizes the surface physical properties of the pure Fe₂O₃ and Fe_{1-y}Mn_yO_x catalysts. Combined with XRD quantitative analysis, the γ Fe₂O₃ ratio in Fe_{1-y}Mn_yO_x catalysts increasing with the Mn mole ratio from 5% to 15%. As summarized in Table 4, the specific surface areas of γ-Fe₂O₃ and γ-Mn₂O₃ are 125 and 55 m²/g, respectively, which is much larger than that of α-Fe₂O₃ (23 m²/g). When doped into α-Fe₂O₃ the Mn mole ratio is 15%, the specific surface area is largest and reaches 85 m²/g, which is enlarge ca. 370% to the α-Fe₂O₃. This shows that the formation of γ-Fe₂O₃ significantly affects the specific surface area of the catalyst. The average pore size of Fe_{0.85}Mn_{0.15}O_x is 14 nm, corresponding to lessen ca. 36% in comparison with the α-Fe₂O₃. Beyond this value, with the Mn mole ratio is increased to 20% the surface area lessened from 85 to 57 m²/g, indicating that doping of excessive manganese may segregate MnO_x nanoparticles lead to the collapse or sintering of the pore structure, will lead to an lessen in the specific surface area of the catalyst. Generally, NO conversion is related to specific surface area of catalyst in NH₃-SCR, as shown in Fig. 1(a). Interestingly, Fe_{0.95}Mn_{0.05}O_x and Fe_{0.90}Mn_{0.10}O_x catalysts have similar specific surface areas, 53 m²/g and 52 m²/g respectively, but the NH₃-SCR activity at low temperature is quite different. The NO conversion of Fe_{0.90}Mn_{0.10}O_x catalyst is 96.6% while Fe_{0.95}Mn_{0.05}O_x

Table 4
Summary of the structural properties of the samples.

Materials	Specific surface area (m ² /g)	Pore volume (cm ³ /g)	Pore Size (nm)
α-Fe ₂ O ₃	23	0.12	22
Fe _{0.95} Mn _{0.05} O _x	53	0.28	18
Fe _{0.90} Mn _{0.10} O _x	52	0.21	17
Fe _{0.85} Mn _{0.15} O _x	85	0.29	14
Fe _{0.80} Mn _{0.20} O _x	57	0.22	16
γ-Fe ₂ O ₃	125	0.45	14
γ-Mn ₂ O ₃	55	0.19	11

catalyst is only 63.6% at 100 °C, which may be related to the magnetism of the catalyst.

3.2.4. SEM and EDS analysis

To elaborate examine the $\text{Fe}_{1-y}\text{Mn}_y\text{O}_x$ and $\alpha\text{-Fe}_2\text{O}_3$ structure, SEM observation were used for understand the structure of the $\alpha\text{-Fe}_2\text{O}_3$ and $\text{Fe}_{0.85}\text{Mn}_{0.15}\text{O}_x$ catalysts and results are shown in Fig. 2(e) and (f). It can be seen that the surface morphology of $\alpha\text{-Fe}_2\text{O}_3$ presents smooth spherical particle accumulation, and its particle size is 1–3 μm . After modified the Fe_2O_3 crystal structure by introducing Mn, the smooth sphere was dispersed into smaller spheres, showing more surface defects, and its particle size was obviously smaller than that of $\alpha\text{-Fe}_2\text{O}_3$. This structural change will increase the specific surface area of the catalyst, which is beneficial to the adsorption of NH_3 and O_2 , thus improving the removal efficiency of NO_x . This result is consistent with N_2 adsorption-desorption curve data and support by $\text{NH}_3\text{/O}_2$ -TPD results. Moreover, EDS mapping were tested to further explore the distribution of Mn species on the $\text{Fe}_{0.85}\text{Mn}_{0.15}\text{O}_x$ catalyst. Fig S4 shows elemental maps of Fe, Mn and O on the $\text{Fe}_{0.85}\text{Mn}_{0.15}\text{O}_x$ catalyst. From the signal intensity of Mn in the Fig S4(d) is much lower than that of Fe, it can be seen that Mn species are highly dispersed in the $\text{Fe}_{0.85}\text{Mn}_{0.15}\text{O}_x$ catalyst. The EDS mapping results also confirm the homogeneous dispersion of Mn species and Fe co-located in the doped samples.

3.3. Redox properties

The redox property of the catalyst is crucial to the $\text{NH}_3\text{-SCR}$ reaction activity at low temperature. For this reason, $\text{H}_2\text{-TPR}$ and $\text{O}_2\text{-TPD}$ was used to analyze the redox property of the $\alpha\text{-Fe}_2\text{O}_3$, $\gamma\text{-Fe}_2\text{O}_3$, $\gamma\text{-Mn}_2\text{O}_3$ and $\text{Fe}_{1-y}\text{Mn}_y\text{O}_x$ catalysts, with the $\text{H}_2\text{-TPR}$ results shown in Fig. 3(a) and H_2 consumption peaks area are summarized in Table 5. All asymmetric peaks are deconvoluted by the by Gaussian-Lorenz function. For the $\alpha\text{-Fe}_2\text{O}_3$, composing only of the octahedral $\text{Fe}^{3+}(\text{Fe}_{\text{Oh}}^{3+})$ sites, two visible peaks are observed at about 381 and 620 °C, which correspond to consecutive reduction process: $\text{Fe}_{(\text{Oh})2}\text{O}_3 \rightarrow \text{Fe}_3\text{O}_4 \rightarrow \text{FeO}$ [28,29]. Different from $\alpha\text{-Fe}_2\text{O}_3$, $\gamma\text{-Fe}_2\text{O}_3$ consisting of $\text{Fe}_{\text{Fd}}^{3+}$ and $\text{Fe}_{\text{Oh}}^{3+}$ sites and $\text{Fe}_{\text{Fd}}^{3+}$ sites is more active in redox reaction at low temperatures [7,9,30,31]. Therefore, $\gamma\text{-Fe}_2\text{O}_3$ has two peaks around 352 and 409 °C, which correspond to the reduction of $\text{Fe}_{(\text{Th})2}\text{O}_3 \rightarrow \text{Fe}_3\text{O}_4$ and $\text{Fe}_{(\text{Oh})2}\text{O}_3 \rightarrow \text{Fe}_3\text{O}_4$, respectively. In addition, the peak around 586 °C corresponds to the reduction of $\text{Fe}_3\text{O}_4 \rightarrow \text{FeO}$ [7,9,30,31]. The two peaks of $\gamma\text{-Mn}_2\text{O}_3$ at 317 and 452 °C correspond to the reduction of $\text{Mn}_2\text{O}_3 \rightarrow \text{Mn}_3\text{O}_4$ and $\text{Mn}_3\text{O}_4 \rightarrow \text{MnO}$, respectively. In comparison with the $\alpha\text{-Fe}_2\text{O}_3$, two reduction peaks at 381 and 620 °C shift to 361 and 556 °C in the $\text{Fe}_{0.85}\text{Mn}_{0.15}\text{O}_x$, respectively. Combine with the $\text{Fe}_{1-y}\text{Mn}_y\text{O}_x$ catalysts XRD and XPS results, spinel structure coupled with two new reduction peak of $\text{Fe}_{1-y}\text{Mn}_y\text{O}_x$ is observed at ~ 297 and 330 °C, which is attribute to the $\text{Mn}_2\text{O}_3 \rightarrow \text{Mn}_3\text{O}_4$ and $\text{Fe}_{(\text{Th})2}\text{O}_3 \rightarrow \text{Fe}_3\text{O}_4$ in $\text{Fe}_{1-y}\text{Mn}_y\text{O}_x$ catalysts. Because the shift of the peak position to a lower temperature represents the improvement of the reduction properties of the catalyst [32]. With increase the Mn^{3+} content from 5% to 15%, it can be apparently observed that the peaks area of $\text{Fe}_{(\text{Oh})2}\text{O}_3 \rightarrow \text{Fe}_3\text{O}_4$ (~380 °C) is decrease and shift to lower temperatures and the peak area of $\text{Mn}_2\text{O}_3 \rightarrow \text{Mn}_3\text{O}_4$ gradually increases at ~300 °C. It suggests that substitution $\text{Fe}_{(\text{Oh})}^{3+}$ with Mn^{3+} to form $\text{Mn}_{(\text{Oh})}^{3+}$ can facilitate the reduction process of $\text{Fe}_{(\text{Oh})}$

$\rightarrow \text{Fe}_3\text{O}_4 \rightarrow \text{FeO}$ by electron transfer between Mn^{3+} and Fe^{3+} . However, there has no obvious influence the reduction peaks area change of $\text{Fe}_{(\text{Th})2}\text{O}_3 \rightarrow \text{Fe}_3\text{O}_4$ (~330 °C), more importantly, the decreasing reduction peak areas of $\text{Fe}_{(\text{Oh})2}\text{O}_3 \rightarrow \text{Fe}_3\text{O}_4$ approximate increasing peak areas of $\text{Mn}_2\text{O}_3 \rightarrow \text{Mn}_3\text{O}_4$, which is significant evidence that the Fe^{3+} sites substituted with Mn^{3+} are $\text{Fe}_{\text{Oh}}^{3+}$ sites rather than $\text{Fe}_{\text{Th}}^{3+}$ sites in $\gamma\text{-Fe}_2\text{O}_3$ of $\text{Fe}_{1-y}\text{Mn}_y\text{O}_x$ catalysts. This is consistent with the previous XRD analysis.

The $\text{O}_2\text{-TPD}$ curves of $\alpha\text{-Fe}_2\text{O}_3$, $\gamma\text{-Fe}_2\text{O}_3$, $\gamma\text{-Mn}_2\text{O}_3$ and $\text{Fe}_{1-y}\text{Mn}_y\text{O}_x$ catalysts are shown in Fig. 3(b). Four O_2 desorption peaks are observed at ~200, ~300, ~450 and ~530 °C in $\alpha\text{-Fe}_2\text{O}_3$ and $\text{Fe}_{1-y}\text{Mn}_y\text{O}_x$ catalysts with the temperature increasing from 100 to 650 °C. For $\gamma\text{-Fe}_2\text{O}_3$, two peaks are observed at 263 and 412 °C, and three peaks appear at 197, 375 and 543 °C were detected in $\gamma\text{-Mn}_2\text{O}_3$. The peaks at ~100–300 °C are assigned to chemically adsorbed oxygen (O_{abs} , O_{abs}) denoted as O_{α} while the peaks at ~300–600 °C are assigned to lattice oxygen (O_{latt}) denoted as O_{β} , among which the O_{α} are related to surface oxygen defect [4]. The O_{α} peaks area and position were summarized in the Table 6, compared with $\gamma\text{-Fe}_2\text{O}_3$, $\alpha\text{-Fe}_2\text{O}_3$ and $\gamma\text{-Mn}_2\text{O}_3$ show small O_{α} peak area, which indicates that $\gamma\text{-Fe}_2\text{O}_3$ has more oxygen vacancies. Furthermore, the $\text{Fe}_{0.85}\text{Mn}_{0.15}\text{O}_x$ exhibits the largest area of O_{α} peak among the $\text{Fe}_{1-y}\text{Mn}_y\text{O}_x$ catalysts. This corresponds to the fact that $\text{Fe}_{0.85}\text{Mn}_{0.15}\text{O}_x$ has the highest content of $\gamma\text{-Fe}_2\text{O}_3$ among the $\text{Fe}_{1-y}\text{Mn}_y\text{O}_x$ catalysts in the previous XRD analysis, showing that introduction of Mn promoted the formation of $\gamma\text{-Fe}_2\text{O}_3$ is conducive to generate more surface oxygen defect. The oxygen defect has been reported that favorable for promoting the redundant electrons transferred to the different metal ions surrounding the oxygen vacancy thus facilitating oxidation of NO to NO_2 [4,33,34], which is in accord with XPS and in-situ DRIFT results.

3.4. Acidity properties

$\text{NH}_3\text{-TPD}$ studies were conducted to characterize the surface acidity of the $\alpha\text{-Fe}_2\text{O}_3$, $\gamma\text{-Fe}_2\text{O}_3$, $\gamma\text{-Mn}_2\text{O}_3$ and $\text{Fe}_{1-y}\text{Mn}_y\text{O}_x$ catalysts. As shown in Fig. 4(a), for $\alpha\text{-Fe}_2\text{O}_3$ and $\gamma\text{-Mn}_2\text{O}_3$, the low intensity peaks are observed at about 210 and 196 °C, respectively, demonstrating the poor NH_3 desorption and less acidic sites of $\alpha\text{-Fe}_2\text{O}_3$ and $\gamma\text{-Mn}_2\text{O}_3$, the profiles of $\text{Fe}_{1-y}\text{Mn}_y\text{O}_x$ catalysts and $\gamma\text{-Fe}_2\text{O}_3$ can be divide into two peaks at ~105 and ~200 °C, previous studies have shown that NH_3 desorption peaks appeared in the range of 100–150 and 150–350 °C are assigned to the physical adsorption of NH_3 and weak acidity, respectively [32,35]. As shown in Fig. 4(b), compared with $\alpha\text{-Fe}_2\text{O}_3$, it was clear that the NH_3 desorption amounts of $\text{Fe}_{1-y}\text{Mn}_y\text{O}_x$ catalysts and $\gamma\text{-Fe}_2\text{O}_3$ were much higher than the $\alpha\text{-Fe}_2\text{O}_3$ and $\gamma\text{-Mn}_2\text{O}_3$, suggesting that incorporation of Mn formation of $\gamma\text{-Fe}_2\text{O}_3$ contribute to the increase of acidic sites on the $\text{Fe}_{1-y}\text{Mn}_y\text{O}_x$ catalysts surface, which can enhance the NO conversion on $\text{Fe}_{1-y}\text{Mn}_y\text{O}_x$ in the $\text{NH}_3\text{-SCR}$ reaction.

It is generally recognized that coordinate NH_2 species and Brønsted acid is decisive for the $\text{NH}_3\text{-SCR}$ LT activity [1,36]. In situ DRIFTS of NH_3 adsorption-desorption is conducted to differentiate Lewis (denoted as L) acid and Brønsted (denoted as B) acid, and the results are shown in Fig. 4(c) and Fig. 4(d). Several bands were appeared after NH_3 coordinated with acidic sites on the $\alpha\text{-Fe}_2\text{O}_3$ and $\gamma\text{-Fe}_2\text{O}_3$ catalyst surface. As the previous studies were shown that the bands appear at 1141, 1225 and 1600 cm^{-1} attributed to NH_3 species adsorbed on the L-acid sites, while the bands at 1351, 1374 and 1553, 1577 cm^{-1} could be classified as the

Table 5
 H_2 consumption peak area of each phase in various catalysts.

Samples	$\text{Fe}_{(\text{Oh})2}\text{O}_3 \rightarrow \text{Fe}_3\text{O}_4$	$\text{Fe}_{(\text{Th})2}\text{O}_3 \rightarrow \text{Fe}_3\text{O}_4$	$\text{Mn}_2\text{O}_3 \rightarrow \text{Mn}_3\text{O}_4$	Total H_2 consumption
$\alpha\text{-Fe}_2\text{O}_3$	3944	–	–	4944
$\text{Fe}_{0.95}\text{Mn}_{0.05}\text{O}_x$	1301	2054	502	3857
$\text{Fe}_{0.90}\text{Mn}_{0.10}\text{O}_x$	953	2024	1016	3993
$\text{Fe}_{0.85}\text{Mn}_{0.15}\text{O}_x$	156	2033	1722	3911
$\text{Fe}_{0.80}\text{Mn}_{0.20}\text{O}_x$	488	2003	1462	3953
$\gamma\text{-Fe}_2\text{O}_3$	2015	4022	–	6037
$\gamma\text{-Mn}_2\text{O}_3$	–	–	4822	4822

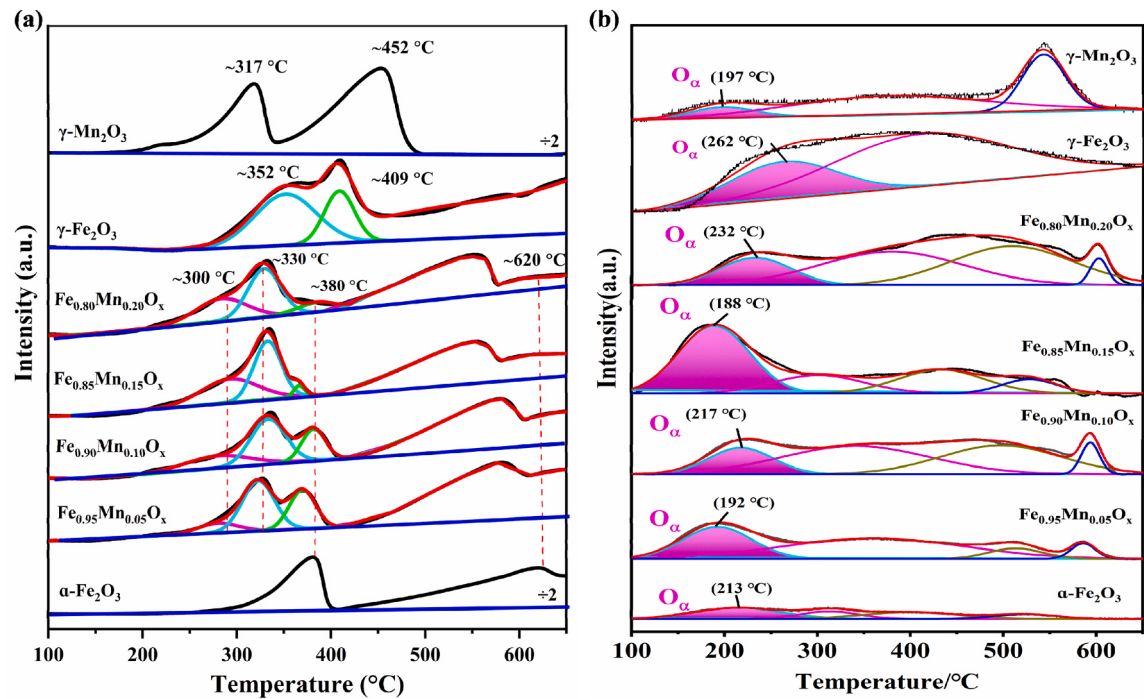
Fig. 3. H₂-TPR (a) and O₂-TPD (b) profiles of catalysts.

Table 6
The O_α peak area and position of catalysts.

Samples	Position (°C)	Area
α-Fe ₂ O ₃	213	494
Fe _{0.95} Mn _{0.05} O _x	192	1122
Fe _{0.90} Mn _{0.10} O _x	217	859
Fe _{0.85} Mn _{0.15} O _x	188	2456
Fe _{0.80} Mn _{0.20} O _x	232	1000
γ-Fe ₂ O ₃	262	2115
γ-Mn ₂ O ₃	197	369

NH₂ species and NH₂ species coordinated to L-acid, respectively [37, 38]. It should be pointed out that the peaks at 1425 and 1462 cm⁻¹ belonging to Brønsted acid site in the γ-Fe₂O₃, which are not observed in the spectrum of α-Fe₂O₃. For the Fe_{0.85}Mn_{0.15}O_x catalyst, the bands appear at 1140, 1194, and 1600 cm⁻¹ could be assigned to the L acid site while the bands at 1451 and 1643 cm⁻¹ are NH₄⁺ ions attached to the B acid site. It is obvious that NH₃ adsorption-desorption bands of α-Fe₂O₃ and Fe_{0.85}Mn_{0.15}O_x are similar but have some differences. Compared with α-Fe₂O₃, Fe_{0.85}Mn_{0.15}O_x has extra acid site 1194 (L acid) and 1451, 1643 cm⁻¹ (B acid), indicating that introduction of Mn formation of γ-Fe₂O₃ is conducive to the formation of B-acid sites. Besides, 1360 and 1573 cm⁻¹ are related to the NH₂⁻ and NH₂ species, respectively. Active NH₂ species from oxidative dehydrogenation of NH₃ are essential intermediates for E-R reaction and establish acid cycle on the catalyst surface [9,17,39]. The bands assigned to NH₂ (1360 cm⁻¹) and NH₂ (1573 cm⁻¹) species can be detected on the surface of Fe_{0.85}Mn_{0.15}O_x and γ-Fe₂O₃ at 50 °C. This shows that the acid cycle of NH₃ and E-R reaction on Fe_{0.85}Mn_{0.15}O_x and γ-Fe₂O₃ can be carried out at a lower temperature than that of α-Fe₂O₃.

3.5. Surface chemical state

The surface atomic composition and valence state distribution of the catalyst are crucial to understand the redox cycle in NH₃-SCR, hence XPS measurements of Fe_{0.85}Mn_{0.15}O_x and α-Fe₂O₃ were conducted and the results are displayed in Fig. 5 and Table 7. All asymmetric peaks are

deconvoluted by the Gaussian-Lorenz function. As displayed in Fig. 5(a), for α-Fe₂O₃, the peaks arise at 709.5 and 711.1 eV, which were attached to Fe²⁺ and Fe³⁺, respectively [4,40,41]. It can be observed that compare to the α-Fe₂O₃, Fe_{0.85}Mn_{0.15}O_x peak position of Fe²⁺ and Fe³⁺, shifted from 709.5 to 709.7 eV and 711.1–711.5 eV higher binding energy, respectively, revealing that exist electrons transferred between Mn and Fe in Fe_{0.85}Mn_{0.15}O_x. This electron transfer and interaction is also reflected in the XRD and H₂-TPR results. Fig. 5(b) shows the XPS spectra of Mn 2p, the peaks located at 641.2 and 643.4 eV were assigned to the Mn³⁺ and Mn⁴⁺, respectively [39]. The O 1 s spectra of α-Fe₂O₃ and Fe_{0.85}Mn_{0.15}O_x in Fig. 5(c) were fitted into two peaks, chemically adsorbed oxygen (O_{ads}⁺, O_{ads}⁻) denoted as O_α (531.6 eV) and lattice oxygen (O_{latt}²⁻) denoted as O_β (529.7 eV) [4,42,43]. Moreover, compared with α-Fe₂O₃, the O_β peak shift from 529.8 to 529.6 eV lower binding energy was detected on Fe_{0.85}Mn_{0.15}O_x sample, which may result from the electron transfer in the strong interaction between Fe-O-Mn after Mn substituting part inactive Fe³⁺ sites of α-Fe₂O₃. As summarized in Table 7, compare Fe_{0.85}Mn_{0.15}O_x and α-Fe₂O₃, the percent of O_α on Fe_{0.85}Mn_{0.15}O_x clearly increases from 15.3% to 45.4%, respectively, which immensely enhances the redox capacity of Fe_{0.85}Mn_{0.15}O_x catalyst. More importantly, compare to Fe_{0.85}Mn_{0.15}O_x, the percent of Fe³⁺ and Mn³⁺ were decrease while the percent of Fe²⁺, Mn⁴⁺ and O_α were increase on A-Fe_{0.85}Mn_{0.15}O_x surface. According to previous researches, the oxygen vacancy by accelerating the transfer of redundant electrons from metal ions (Fe³⁺, Mn³⁺) hence facilitating the formation of Fe²⁺ and Mn⁴⁺ ions, which is consistent with our experimental observation and proves that the redox cycle between Fe³⁺ + Mn³⁺ ↔ Fe²⁺ + Mn⁴⁺ of Fe_{0.85}Mn_{0.15}O_x exist in NH₃-SCR reaction.

3.6. In-situ DRIFT tests

3.6.1. NO + O₂ adsorption-desorption

In-situ DRIFTS test of NO+O₂ adsorption-desorption were carried out due to investigate the NO_x active species on the catalyst surface at different temperatures is indispensable for revealing the reaction mechanism. As shown in Fig. 6(a), the surface of α-Fe₂O₃ adsorbed species of linear nitrite (1078 cm⁻¹), monodentate nitrate (1286 cm⁻¹) and bridged nitrate (1600 cm⁻¹) are observed at 50 °C. As the

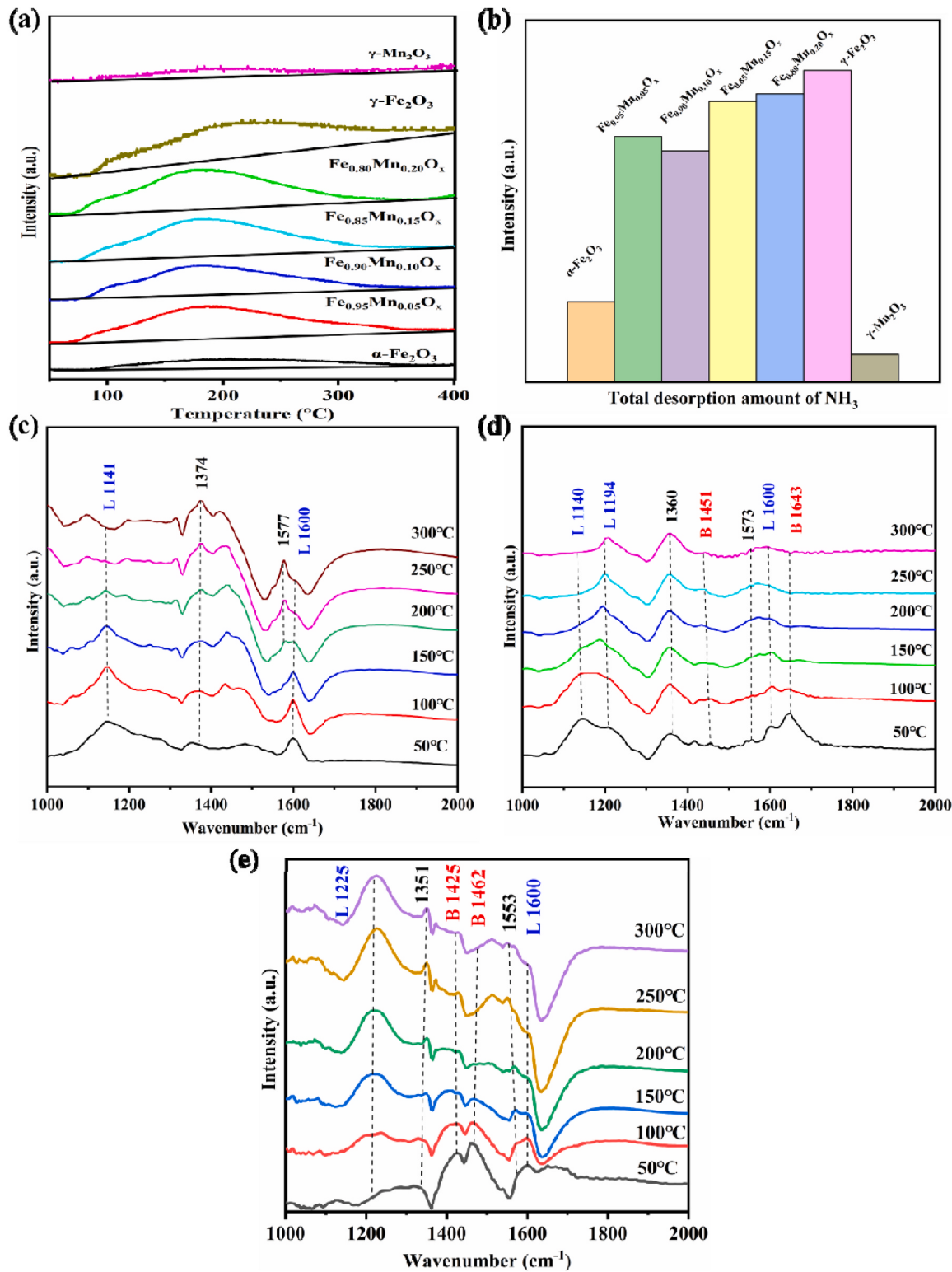


Fig. 4. (a) NH₃-TPD patterns of catalysts; (b) Total desorption amount of NH₃; In-situ DRIFTS spectra of NH₃ adsorption-desorption: (c) α -Fe₂O₃, (d) Fe_{0.85}Mn_{0.15}O_x and (e) γ -Fe₂O₃.

temperature rises, the intensity of monodentate nitrate weaken while new peaks of bidentate nitrate (1547, 1570 cm⁻¹) and bridged nitrite (1206 cm⁻¹) are observed at 150–300 °C [8,35,44]. The results show that with the increase of temperature, monodentate nitrate species gradually transforms into quite stable NO_x species. Distinguish from α -Fe₂O₃, the bands of monodentate nitrate (1436 cm⁻¹) can form on γ -Fe₂O₃ surface at 50 °C. Besides, with the temperature rises from 150 to

300 °C, all the bands intensity significant weaken, which indicate that NO_x species formed on the surface of γ -Fe₂O₃ are unstable at 150–300 °C. For Fe_{0.85}Mn_{0.15}O_x, as exhibited in Fig. 6(b), the bands relating to bridged nitrite (1197 cm⁻¹), NO₂ (1622 cm⁻¹) and monodentate nitrate (1434 cm⁻¹) can be observed on the Fe_{0.85}Mn_{0.15}O_x surface at 50 °C, indicating that the NO₂ and bridged nitrite can be generated from oxidation of NO at low temperatures. Among active NO_x species, NO₂

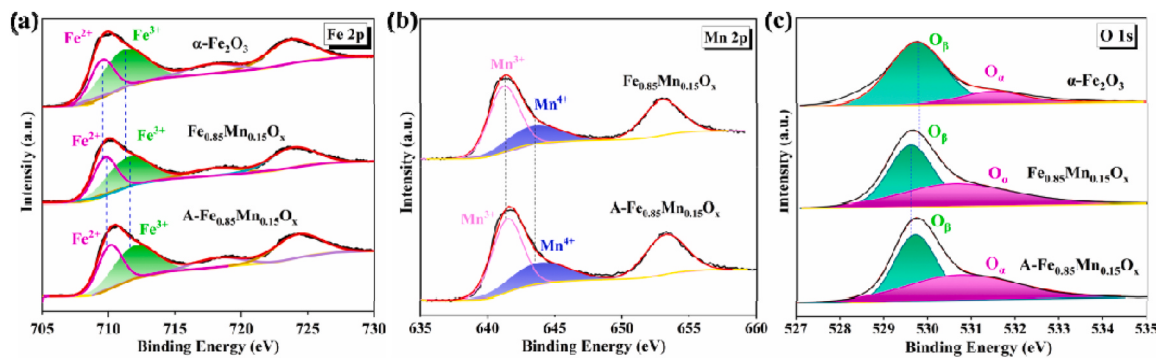


Fig. 5. XPS spectra of Fe_{0.85}Mn_{0.15}O_x (after NH₃-SCR reaction denoted as A-Fe_{0.85}Mn_{0.15}O_x) and α-Fe₂O₃: (a) Fe 2p, (b) Mn 2p, (c) O1s.

Table 7

Surface atomic concentration of Fe_{0.85}Mn_{0.15}O_x (after NH₃-SCR reaction denoted as A-Fe_{0.85}Mn_{0.15}O_x) and α-Fe₂O₃.

Samples	Atomic Concentration (mol%)	Fe _{total}	Mn _{total}	O _{total}
α-Fe ₂ O ₃		28.5	—	71.5
Fe _{0.85} Mn _{0.15} O _x		19.9	10.5	69.6
A-Fe _{0.85} Mn _{0.15} O _x		19.9	10.7	69.4
Atomic Ratio (%)		Fe ³⁺ / (Fe _{total})	Fe ²⁺ / (Fe _{total})	Mn ⁴⁺ / (Mn _{total})
α-Fe ₂ O ₃		65.5	34.5	—
Fe _{0.85} Mn _{0.15} O _x		58.8	41.2	65.9
A-Fe _{0.85} Mn _{0.15} O _x		57.4	42.6	34.1
				36.2
				48.8
				51.2

from NO oxidation can significantly boost LT NH₃-SCR activity by inducing Fast SCR reaction [45,46]. Moreover, the bridged nitrite (1197 cm⁻¹) and NO₂ (1622 cm⁻¹) decrease with increasing temperature and then vanish at 200 °C, while the peak intensity of bridged nitrate (1248 cm⁻¹) and bidentate nitrate (1572 cm⁻¹) arise at 150 °C, indicating that bridged nitrite can be transform to bridged nitrate and bidentate nitrate at 150 °C. Previous study indicated bidentate nitrates are inactive at low temperatures while became active at high temperatures [47]. It is worth noting that monodentate nitrate, bridged nitrate and bidentate nitrate weaken with the temperatures over 200 °C, indicating that NO_x species more easier form equilibrium of formation-decomposition on Fe_{0.85}Mn_{0.15}O_x surface than α-Fe₂O₃ at 50–300 °C. This phenomenon is similar to the γ-Fe₂O₃ and consistent with the previously reported that magnetism affects the adsorption of NO at low temperature and the analysis of our VSM experimental results. Commonly, the SCR activity decrease with formation of steady NO_x species by cause of covering active sites on the catalyst surface [48]. This discrepancy formation of NO_x species and its thermal stability on the Fe_{0.85}Mn_{0.15}O_x and α-Fe₂O₃ surface may be one of the crucial factors leading to the excellent LT NH₃-SCR activity of Fe_{0.85}Mn_{0.15}O_x at 50–300 °C.

3.6.2. NH₃+NO+O₂ co-adsorption

The reaction mechanism of α-Fe₂O₃, γ-Fe₂O₃ and Fe_{0.85}Mn_{0.15}O_x was further investigated by NH₃+NO+O₂ co-adsorption. As shown in Fig. 7 (a), several bands assigned to linear nitrite (1080 cm⁻¹), monodentate nitrate (1282, 1482 cm⁻¹), bridged nitrate (1226, 1609 cm⁻¹), NH₂ species (1572 cm⁻¹) and bridged nitrite (1202 cm⁻¹) can be observed on the α-Fe₂O₃ of NH₃+NO+O₂ co-adsorption. However, the bands relevant to NH₃ adsorption didn't appear and the monodentate nitrate and bridged nitrite species quite stable on the α-Fe₂O₃ surface at below 150 °C. According to previous research, competitive adsorption between NH₃ and NO+O₂ exists and NO+O₂ was on α-Fe₂O₃ preferential adsorption [8,47]. That means that the adsorbed NO_x species and NH₃ is difficult to occur reaction on α-Fe₂O₃ at low temperatures. As shown in Fig. 7(a), compared with α-Fe₂O₃, the bands attribute to NH₄⁺ ions coordinated with B-acid sites (1438 cm⁻¹), NH₂ (1364 cm⁻¹) and NH₂

species (1572 cm⁻¹) can observe on γ-Fe₂O₃ surface at 50 °C. In addition, the bands intensity relevant to NH₃ adsorption gradually weakened and disappeared at 200°C, which indicates that the acidic sites formed on γ-Fe₂O₃ surface can react with NO_x species. After Mn modified Fe₂O₃, as shown in Fig. 7(b), the bands corresponding to bridged nitrite (1206 cm⁻¹), NO₂ (1614 cm⁻¹), NH₄⁺ ions coordinated with B-acid sites (1465 cm⁻¹), NH₂ (1364 cm⁻¹), NH₂ specie (1516 cm⁻¹) and NH₄NO₂ (1078 cm⁻¹) can be observed on the Fe_{0.85}Mn_{0.15}O_x surface at 50 °C. Furthermore, the peaks intensity of bridged nitrite, NH₄⁺ ions and NO₂ rapidly decline from 50 to 100 °C, indicating that the Fast SCR reaction is able to occur on Fe_{0.85}Mn_{0.15}O_x at low temperature. Besides, the overlapping peaks of NH₂ species (1516 cm⁻¹) and NH₄⁺ ions coordinated with B-acid sites (1465 cm⁻¹) at 200–300 °C were identified. Remarkably, there is no bands relevant to NO+O₂ while the bands intensity corresponding to NH₃ coordinated with the L-acid and B-acid sites became stronger with temperature from 200 to 300 °C, which is mainly because high temperature promotes the oxidative dehydrogenation of NH₃ on Fe_{0.85}Mn_{0.15}O_x.

3.6.3. Reactivity of adsorbed species on Fe_{0.85}Mn_{0.15}O_x

In-situ DRIFTS instantaneous reaction were proposed to explore the reaction intermediates of Fe_{0.85}Mn_{0.15}O_x in low temperature NH₃-SCR reaction. The NH₃ was pre-adsorbed on Fe_{0.85}Mn_{0.15}O_x surface for 1 h at 100 °C and NO+O₂ was introduced to react with the adsorbed NH₃ species after the N₂ purge for 0.5 h. As shown in Fig. 8(a), several bands assigned to coordinated NH₃ with L-acid (1086, 1120, and 1602 cm⁻¹), NH₄⁺ ions adsorbed on B-acid sites (1640 cm⁻¹) and N-H vibration of the adsorbed NH₃ (3374 cm⁻¹) can be observed on the Fe_{0.85}Mn_{0.15}O_x surface after adsorption of NH₃ [8,35,44,47]. Moreover, with introducing NO+O₂ that the bands attributed to NH₃ species disappear immediately and the wide bands attributed to O-H (3400–3600 cm⁻¹) was emerged gradually, showing that the introduced NO can directly react with the adsorbed ammonia species to occur Eley-Ridea (E-R) reaction pathway at low temperatures. Furthermore, the bands attributing to NO₂ (1626 cm⁻¹) can be detected gradually (3 min later), according to previous research which can react with NH₄⁺ to occur Langmuir-Hinshelwood (L-H) reaction pathway and then form NH₄NO₂

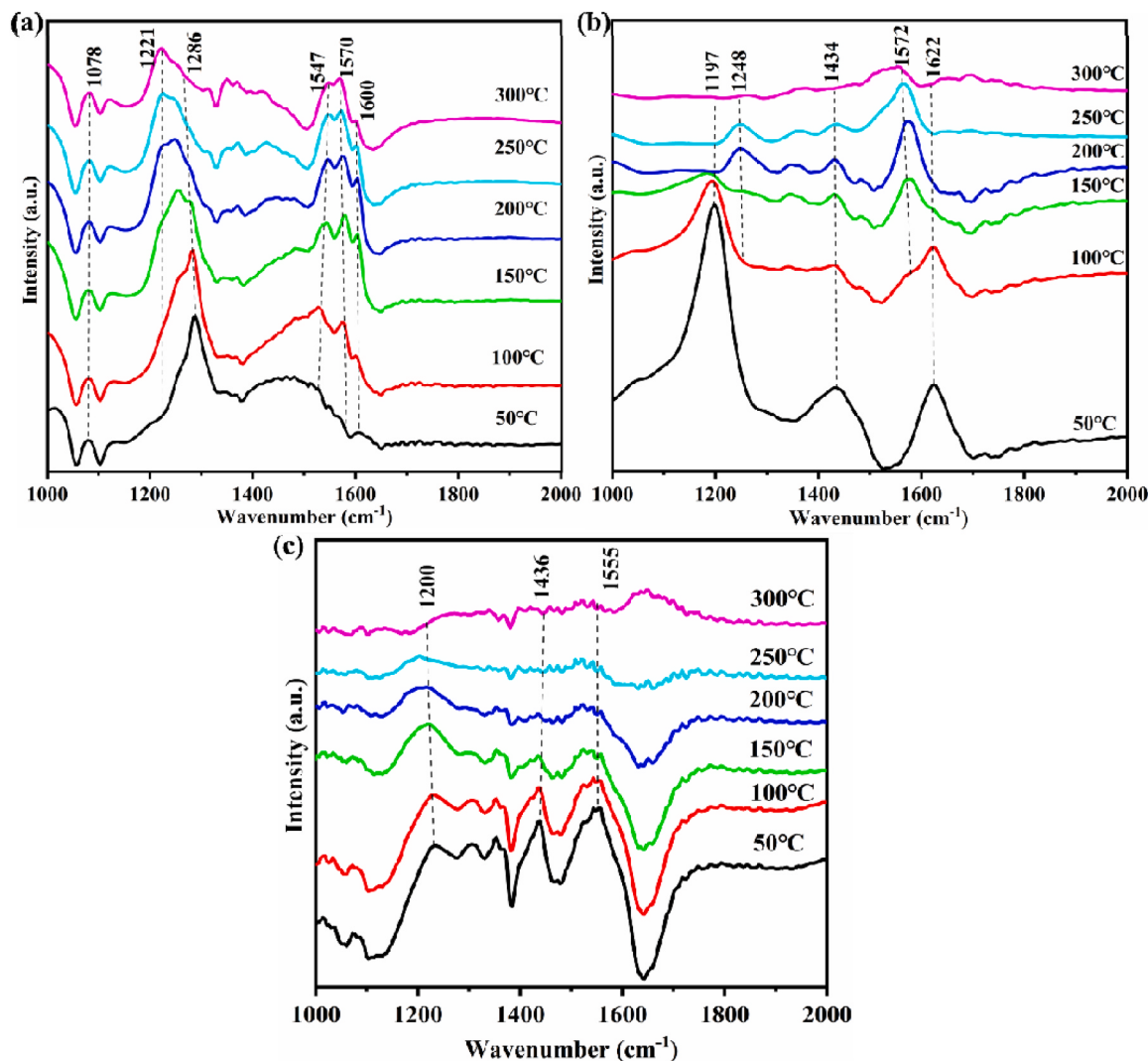


Fig. 6. In-situ DRIFTS spectra of $\text{NO} + \text{O}_2$ adsorption-desorption for catalysts: (a) $\alpha\text{-Fe}_2\text{O}_3$, (b) $\text{Fe}_{0.85}\text{Mn}_{0.15}\text{O}_x$ and (c) $\gamma\text{-Fe}_2\text{O}_3$.

that rapid generation of N_2 and H_2O (Fast SCR).

The transformation between adsorbed NH_3 species and reaction with pre-adsorbed NO_x species is further studied by in-situ DRIFTS studies that $\text{NO} + \text{O}_2$ pre-adsorbed and followed by NH_3 adsorption on $\text{Fe}_{0.85}\text{Mn}_{0.15}\text{O}_x$ at 100 °C. As shown in Fig. 8(b), the bridged nitrite (1194 cm^{-1}) and NO_2 (1621 cm^{-1}) are clearly observed on $\text{Fe}_{0.85}\text{Mn}_{0.15}\text{O}_x$ surface after $\text{NO} + \text{O}_2$ pre-adsorbed. When the NH_3 is introduced, the bands of bridged nitrite, NO_2 and O-H ($3400\text{--}3600\text{ cm}^{-1}$) vanish gradually and several bands assigned to coordinated NH_3 with L-acid sites (1154 , 1254 , 1284 and 1602 cm^{-1}), N-H (3374 cm^{-1}) and NH_4^+ ions adsorbed on B-acid sites (1445 , 1631 cm^{-1}) can be observed [8,32, 35,38]. Furthermore, NH_2 (1565 cm^{-1}) can be detected after 1 min, indicating that NH_3 can be rapidly oxidized to active NH_2 at low temperature. [31,32,47]. Notably, compare with Fig. 8(a), the bands intensity of B-acid sites (1445 cm^{-1}) and NH_2 (1565 cm^{-1}) are obvious became stronger than NH_3 species adsorption alone, indicating that chemically adsorbed oxygen and adsorbed NO_x species is promotes the formation of B-acid sites and NH_2 . Moreover, the intensity of NH_2 (1565 cm^{-1}) gradually weaken while the B-acid sites (1445 cm^{-1}) became stronger in 5 min, indicating that the conversion between NH_2 (1565 cm^{-1}) and B-acid sites (1445 cm^{-1}) in the acid cycle.

3.7. Reaction mechanism

After substituted part inactive Fe^{3+} sites of Fe_2O_3 with active $\text{Mn}^{3+}_{\text{OH}}$, the Fe_2O_3 crystal structure generate more active Fe^{3+} CASs. The establishment of redox cycle $\text{Fe}^{3+} + \text{Mn}^{3+} \leftrightarrow \text{Fe}^{2+} + \text{Mn}^{4+}$ between Fe-O-Mn induced the increase of chemically adsorbed oxygen on the $\text{Fe}_{0.85}\text{Mn}_{0.15}\text{O}_x$ surface, not only boosted the formation of NO_2 but also facilitated the Brønsted acid circle. Based on the results analysis, possible a reaction mechanism that over $\text{Fe}_{0.85}\text{Mn}_{0.15}\text{O}_x$ are proposed and the model are depicted in Fig. 9. In this mechanism, chemisorbed oxygen (O_{abs}) reacts with $\text{Fe}(\text{III})$ to form the $\text{Fe}(\text{III})-\text{O}^-$ reactive intermediates. Subsequently, NH_3 adsorbed on $\text{Fe}(\text{III})-\text{O}^-$ groups proceed oxidative dehydrogenation reaction to produce active $\text{Fe}(\text{III})-\text{OH}-\text{NH}_2$ intermediates. The activated $-\text{NH}_2$ groups derived from $\text{Fe}(\text{III})-\text{OH}-\text{NH}_2$ intermediates could occur Eley-Rideal (E-R) reaction pathway with gaseous NO to generate NH_2-NO intermediate that generation of N_2 , H_2O and generate $\text{Fe}(\text{III})-\text{OH}$ sites. The NH_3 adsorbed on $\text{Fe}(\text{III})-\text{OH}$ sites to occur redox reaction and then form $\text{Fe}(\text{II})-\text{ONH}_4^+$ sites. This catalytic reaction process included the electronic transfer the redox cycle between $\text{Fe}^{3+} + \text{Mn}^{3+} \leftrightarrow \text{Fe}^{2+} + \text{Mn}^{4+}$, the NO_2 is induced to form at low temperature and then reaction with the $\text{Fe}(\text{II})-\text{ONH}_4^+$ to have Fast SCR. The active $\text{Fe}(\text{III})-\text{O}^-$ groups were regenerated through the redox cycle between $\text{Fe}^{3+} + \text{Mn}^{3+} \leftrightarrow \text{Fe}^{2+} + \text{Mn}^{4+}$ to complete redox circle and acid cycle. This cycle also occurs at the $\text{Mn}^{3+}_{\text{OH}}$ active sites.

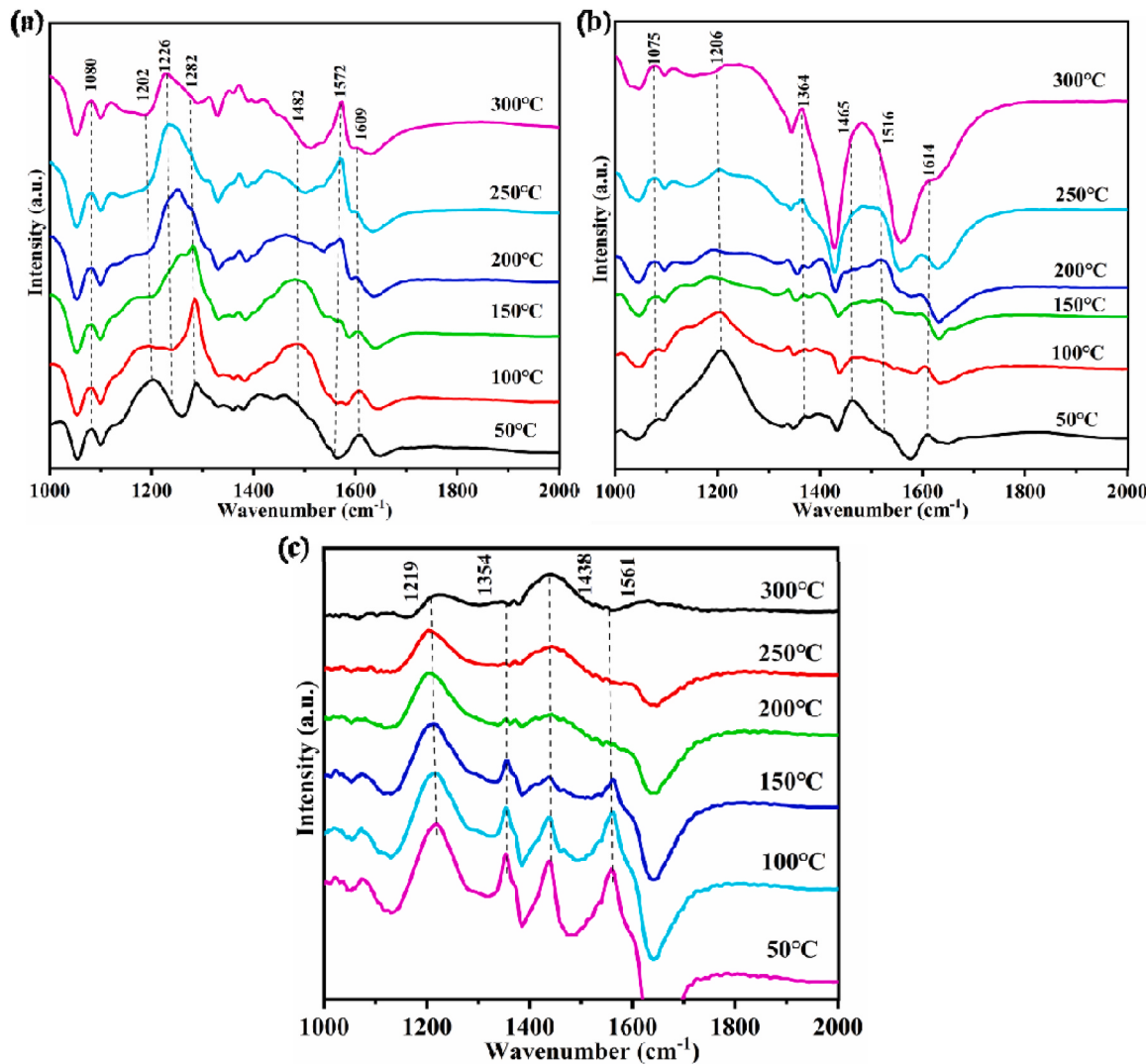


Fig. 7. In-situ DRIFTS spectra of (a) $\alpha\text{-Fe}_2\text{O}_3$, (b) $\text{Fe}_{0.85}\text{Mn}_{0.15}\text{O}_x$ and (c) $\gamma\text{-Fe}_2\text{O}_3$ NH₃+NO+O₂ co-adsorption.

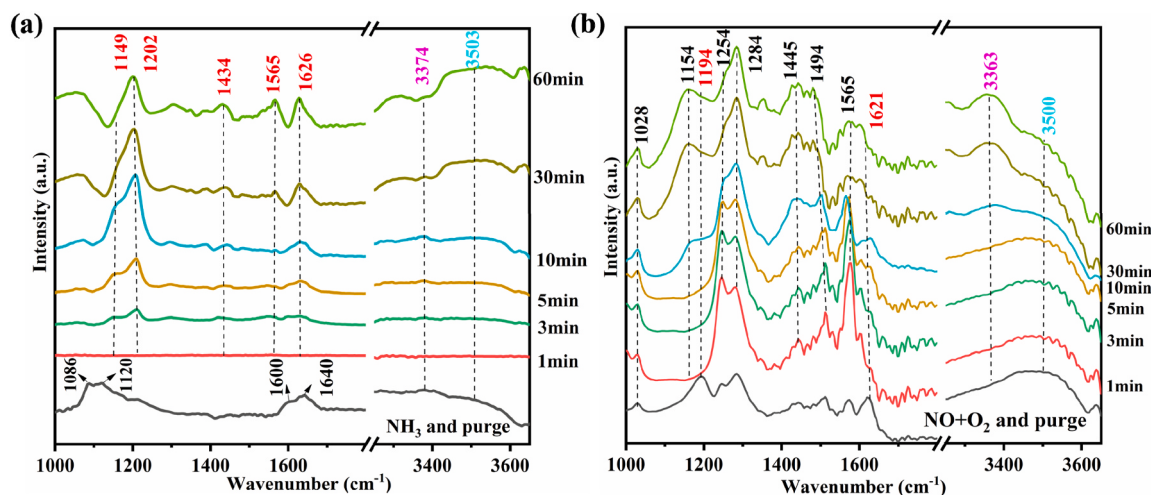


Fig. 8. In-situ DRIFTS spectra of $\text{Fe}_{0.85}\text{Mn}_{0.15}\text{O}_x$ at 100 °C. (a) NH₃ pre-adsorption and then introduced NO+O₂, (b) NO+O₂ pre-adsorption and then introduced NH₃.

4. Conclusions

In this work, a highly LT NH₃-SCR activity and an extensive reaction

window catalyst by Mn modified the $\alpha\text{-Fe}_2\text{O}_3$ crystal structure has been composed by using sol-gel strategy. The transition of $\alpha\text{-Fe}_2\text{O}_3$ to the $\gamma\text{-Fe}_2\text{O}_3$ structure and magnetic properties are promoted after

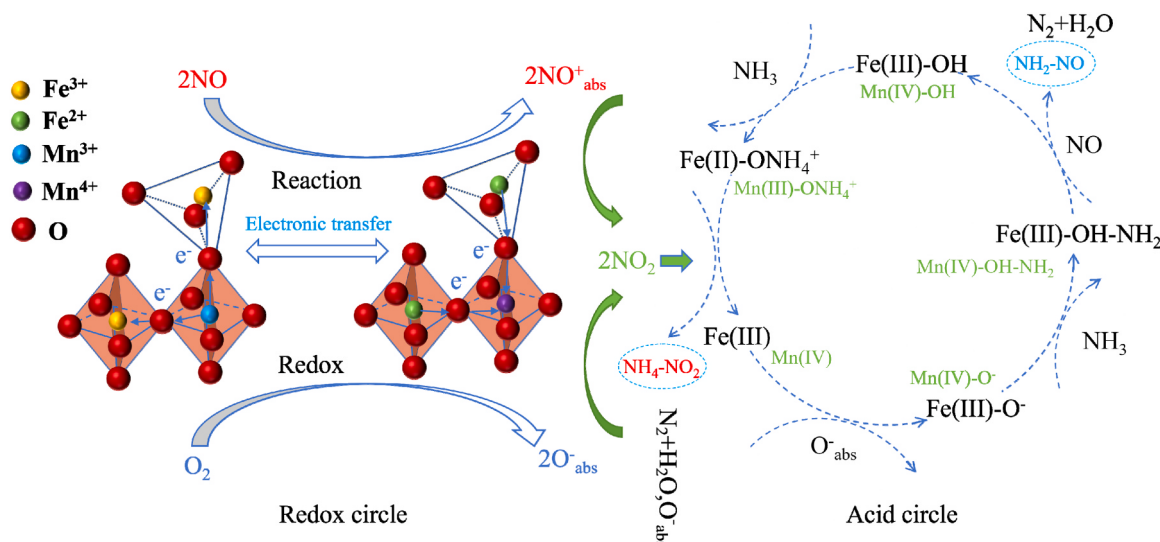


Fig. 9. Reaction mechanism model for $\text{Fe}_{0.85}\text{Mn}_{0.15}\text{O}_x$.

substituted part inactive $\text{Fe}_{\text{O}h}^{3+}$ sites of Fe_2O_3 with active $\text{Mn}_{\text{O}h}^{3+}$ sites. Besides, introducing of highly dispersed Mn^{3+} into the $\gamma\text{-Fe}_2\text{O}_3$ crystalline structure to generate Fe-O-Mn coordinate sites, which can increase of chemically adsorbed oxygen and then enhanced the oxidation of NO and NH_3 on the $\text{Fe}_{0.85}\text{Mn}_{0.15}\text{O}_x$ surface to facilitate the redox circle and acid cycle at low temperatures. It is of great significance to deepen the understanding relationship between crystal structure and CASs of $\alpha\text{-Fe}_2\text{O}_3$ and $\gamma\text{-Fe}_2\text{O}_3$, designing of high-performance catalysts of SCR catalysts at low temperatures.

CRediT authorship contribution statement

Donghai Mo: Conceptualization, Investigation, Methodology, Formal analysis, Writing – original draft, Data curation. **Qiuju Qin:** Resources, Formal analysis, Validation, Visualization. **Chengheng Huang:** Validation, Formal analysis, Software, Visualization. **Lin Tao:** Software, Visualization, Resources. **Chen Li:** Validation, Formal analysis. **Jiaqi Qiu:** Validation, Visualization. **Jingkai Wang:** Formal analysis, Software. **Xiaorong Han:** Validation, Visualization. **Shifei Gu:** Validation, Visualization. **Zhengjun Chen:** Funding acquisition, Supervision. **Bin Li:** Funding acquisition, Supervision. **Lihui Dong:** Funding acquisition, Project administration, Supervision.

Declaration of Competing Interest

The authors declare that they have no known competing financial interests or personal relationships that could have appeared to influence the work reported in this paper.

Data Availability

Data will be made available on request.

Acknowledgments

This work is supported by National Natural Science Foundation of China (No. 22265002, 22062002).

Appendix A. Supporting information

Supplementary data associated with this article can be found in the online version at [doi:10.1016/j.apcatb.2024.123869](https://doi.org/10.1016/j.apcatb.2024.123869).

References

- [1] L. Han, S. Cai, M. Gao, J.-Y. Hasegawa, P. Wang, J. Zhang, L. Shi, D. Zhang, Selective catalytic reduction of NOx with NH3 by using novel catalysts: state of the art and future prospects, *Chem. Rev.* 119 (2019) 10916–10976, <https://doi.org/10.1021/acs.chemrev.9b00202>.
- [2] C.-H. Zheng, C.-R. Xu, X. Gao, Y.-X. Zhang, J. Zhang, Z.-Y. Luo, K.-F. Cen, Simultaneous absorption of NOx and SO2 in oxidant-enhanced limestone slurry, *Environ. Prog. Sustain.* 33 (2014) 1171–1179, <https://doi.org/10.1002/ep.11903>.
- [3] Y. Peng, J. Li, X. Huang, X. Li, W. Su, X. Sun, D. Wang, J. Hao, Deactivation mechanism of potassium on the $\text{V}_2\text{O}_5/\text{CeO}_2$ Catalysts for SCR reaction: acidity, reducibility and adsorbed-NOx, *Environ. Sci. Technol.* 48 (2014) 4515–4520, <https://doi.org/10.1021/es405602a>.
- [4] W. Chen, S. Yang, H. Liu, F. Huang, Q. Shao, L. Liu, J. Sun, C. Sun, D. Chen, L. Dong, Single-Atom Ce-modified $\alpha\text{-Fe}_2\text{O}_3$ for selective catalytic reduction of NO with NH3, *Environ. Sci. Technol.* 56 (2022) 10442–10453, <https://doi.org/10.1021/acs.est.2c02916>.
- [5] X. Tang, Y. Shi, F. Gao, S. Zhao, H. Yi, Z. Xie, Promotional role of Mo on $\text{Ce}_0.3\text{FeO}_x$ catalyst towards enhanced NH3-SCR catalytic performance and SO2 resistance, *Chem. Eng. J.* 398 (2020) 125619, <https://doi.org/10.1016/j.cej.2020.125619>.
- [6] L. Machala, J. Tucek, R. Zboril, Polymorphous transformations of nanometric Iron (III) oxide: a review, *Chem. Mater.* 23 (2011) 3255–3272, <https://doi.org/10.1021/cm200397g>.
- [7] W. Qu, Y. Chen, Z. Huang, J. Gao, M. Zhou, J. Chen, C. Li, Z. Ma, J. Chen, X. Tang, Active Tetrahedral Iron Sites of $\gamma\text{-Fe}_2\text{O}_3$ Catalyzing NO Reduction by NH3, *Environ. Sci. Technol. Lett.* 4 (2017) 246–250, <https://doi.org/10.1021/acs.estlett.7b00124>.
- [8] C. Liu, S. Yang, L. Ma, Y. Peng, A. Hamidreza, H. Chang, J. Li, Comparison on the performance of $\alpha\text{-Fe}_2\text{O}_3$ and $\gamma\text{-Fe}_2\text{O}_3$ for selective catalytic reduction of nitrogen oxides with ammonia, *Catal. Lett.* 143 (2013) 697–704, <https://doi.org/10.1007/s10562-013-1017-3>.
- [9] W. Zhang, X. Shi, Z. Yan, Y. Shan, Y. Zhu, Y. Yu, H. He, Design of high-performance iron-niobium composite oxide catalysts for NH3-SCR: insights into the interaction between Fe and Nb, *ACS Catal.* 11 (2021) 9825–9836, <https://doi.org/10.1021/acscatal.1c01619>.
- [10] G. Xu, X. Guo, X. Cheng, J. Yu, B. Fang, A review of Mn-based catalysts for low-temperature NH3-SCR: NOx removal and H2O/SO2 resistance, *Nanoscale* 13 (2021) 7052–7080, <https://doi.org/10.1039/d1nr00248a>.
- [11] S. Cai, D. Zhang, L. Shi, J. Xu, L. Zhang, L. Huang, H. Li, J. Zhang, Porous Ni-Mn oxide nanosheets in-situ formed on nickel foam as 3D hierarchical monolith de-NOx catalysts, *Nanoscale* 6 (2014) 7346–7353, <https://doi.org/10.1039/c4nr00475b>.
- [12] P. Sun, R.-T. Guo, S.-M. Liu, S.-X. Wang, W.-G. Pan, M.-Y. Li, The enhanced performance of MnOx catalyst for NH3-SCR reaction by the modification with Eu, *Appl. Catal. A* 531 (2017) 129–138, <https://doi.org/10.1016/j.apcata.2016.10.027>.
- [13] Z. Chen, Q. Yang, H. Li, X. Li, L. Wang, S.C. Tsang, Cr-MnOx mixed-oxide catalysts for selective catalytic reduction of NOx with NH3 at low temperature, *J. Catal.* 276 (2010) 56–65, <https://doi.org/10.1016/j.jcat.2010.08.016>.
- [14] H. Chang, X. Chen, J. Li, L. Ma, C. Wang, C. Liu, J.W. Schwank, J. Hao, Improvement of activity and SO2 tolerance of Sn-modified MnOx-CeO2 catalysts for NH3-SCR at low temperatures, *Environ. Sci. Technol.* 47 (2013) 5294–5301, <https://doi.org/10.1021/es304732h>.
- [15] J.R. Lai, K. Shafi, K. Loos, A. Ulman, Y. Lee, T. Vogt, C. Estournès, Doping $\gamma\text{-Fe}_2\text{O}_3$ nanoparticles with Mn(III) suppresses the transition to the $\alpha\text{-Fe}_2\text{O}_3$ structure, *J. Am. Chem. Soc.* 125 (2003) 11470–11471, <https://doi.org/10.1021/ja035409d>.

[16] Y. Wang, L. Chen, W. Wang, X. Wang, B. Li, S. Zhang, W. Li, S. Li, Revealing the excellent low-temperature activity of the $\text{Fe1-xCexO}_8\text{-S}$ catalyst for NH3-SCR: improvement of the lattice oxygen mobility, *ACS Appl. Mater. Interfaces* 15 (2023) 17834–17847. <https://doi.org/10.1021/acsami.3c00212>.

[17] N. Zhu, W. Shan, Z. Lian, Y. Zhang, K. Liu, H. He, A superior Fe-V-Ti catalyst with high activity and SO2 resistance for the selective catalytic reduction of NOx with NH3, *J. Hazard. Mater.* 382 (2020) 120970. <https://doi.org/10.1016/j.jhazmat.2019.120970>.

[18] F. Wang, Z. Xie, J. Liang, B. Fang, Y.a. Piao, M. Hao, Z. Wang, Tourmaline-modified FeMnTiO_x catalysts for improved low-temperature NH3-SCR performance, *Environ. Sci. Technol.* 53 (2019) 6989–6996. <https://doi.org/10.1021/acs.est.9b02620>.

[19] G. Wang, Y. Zhang, J. Lu, Y. Liu, M. Yang, G. Peng, L. Jia, H. Wang, F. Xia, Q. Zhang, The improving effect of SO42- on environmental-friendly SO42-/ α -Fe2O3 catalyst for NH3-SCR, *J. Energy. Inst.* 110 (2023). <https://doi.org/10.1016/j.joei.2023.101347>.

[20] Y. Liu, B. Huang, J. Zhang, Y. Chen, J. Chen, J. Wang, Improved NH3-SCR activity by the cooperation of FeVO_4 and CeO_2 nanosheet catalysts: structure and mechanism, *Catal. Sci. Technol.* 13 (2023) 5374–5386. <https://doi.org/10.1039/d3cy00597f>.

[21] J. Xu, H. Shen, X. Zhou, T. Zheng, F. Guo, Q. Zhang, M. Duan, Enhancement low-temperature NH3-SCR activity of the Fe-Mn-Mo/TiO2 catalyst and its DFT calculations and kinetics, *Mol. Catal.* 551 (2023) 113657. <https://doi.org/10.1016/j.mcat.2023.113657>.

[22] X. Yao, Z. Wang, S. Yu, F. Yang, L. Dong, Acid pretreatment effect on the physicochemical property and catalytic performance of CeO_2 for NH3-SCR, *Appl. Catal. A* 542 (2017) 282–288. <https://doi.org/10.1016/j.apcata.2017.06.003>.

[23] X. Shi, J. Guo, T. Shen, A. Fan, S. Yuan, J. Li, Enhancement of Ce doped La-Mn oxides for the selective catalytic reduction of NOx with NH3 and SO2 and/or H2O resistance, *Chem. Eng. J.* 421 (2021) 129995. <https://doi.org/10.1016/j.cej.2021.129995>.

[24] R. Nikam, S. Rayaprol, S. Mukherjee, S.D. Kaushik, P.S. Goyal, P.D. Babu, S. Radha, V. Siruguri, Structure and magnetic properties of Mn doped α -Fe2O3, *Phys. B Condens. Matter.* 574, 411663. <https://doi.org/10.1016/j.physb.2019.411663>.

[25] C. Wang, S. Yang, H. Chang, Y. Peng, J. Li, Structural effects of iron spinel oxides doped with Mn, Co, Ni and Zn on selective catalytic reduction of NO with NH3, *J. Mol. Catal. A* 376 (2013) 13–21. <https://doi.org/10.1016/j.molcata.2013.04.008>.

[26] R. Zhao, X. Wei, B. Chu, K. Chen, Q. Qin, H. Liu, Y. Zhou, B. Li, L. Dong, Multi-phase coexisting metal oxide derived by MOFs for the CO-SCR reaction at low temperature and in situ DRIFTS study on reaction mechanism, *Appl. Surf. Sci.* 580 (2022) 152277. <https://doi.org/10.1016/j.apsusc.2021.152277>.

[27] S. Xie, L. Li, L. Jin, Y. Wu, H. Liu, Q. Qin, X. Wei, J. Liu, L. Dong, B. Li, Low temperature high activity of M (M = Ce, Fe, Co, Ni) doped M-Mn/TiO2 catalysts for NH3-SCR and in situ DRIFTS for investigating the reaction mechanism, *Appl. Surf. Sci.* 515 (2020) 146014. <https://doi.org/10.1016/j.apsusc.2020.146014>.

[28] S. Yang, C. Liu, H. Chang, L. Ma, Z. Qu, N. Yan, C. Wang, J. Li, Improvement of the activity of γ Fe2O3 for the selective catalytic reduction of NO with NH3 at high temperatures: NO reduction versus NH3 oxidation, *Ind. Eng. Chem. Res.* 52 (2013) 5601–5610. <https://doi.org/10.1021/ie303272u>.

[29] J. Sun, Y. Lu, L. Zhang, C. Ge, C. Tang, H. Wan, L. Dong, Comparative study of different doped metal cations on the reduction, acidity, and activity of Fe9M1O_x (M = Ti4+, Ce4+/3+, Al3+) catalysts for NH3-SCR reaction, *Ind. Eng. Chem. Res.* 56 (2017) 12101–12110. <https://doi.org/10.1021/acs.iecr.7b03080>.

[30] C. Li, Z. Huang, Y. Chen, X. Liu, J. Chen, W. Qu, Z. Ma, X. Tang, Optimizing selective catalytic reduction of NO with NH3 on Fe2O3/WO3 via redox-acid synergy, *Chemcatchem* 10 (2018) 3990–3994. <https://doi.org/10.1002/cctc.201801070>.

[31] Z. Chen, F. Wang, H. Li, Q. Yang, L. Wang, X. Li, Low-temperature selective catalytic reduction of NOx with NH3 over Fe-Mn mixed-oxide catalysts containing Fe3Mn3O8 phase, *Ind. Eng. Chem. Res.* 51 (2012) 202–212. <https://doi.org/10.1021/ie201894c>.

[32] H. Hu, S. Cai, H. Li, L. Huang, L. Shi, D. Zhang, In Situ DRIFTS investigation of the low-temperature reaction mechanism over Mn-doped Co3O4 for the selective catalytic reduction of NOx with NH3, *J. Phys. Chem. C* 119 (2015) 22924–22933. <https://doi.org/10.1021/acs.jpcc.5b06057>.

[33] S. Xie, Q. Qin, H. Liu, L. Jin, X. Wei, J. Liu, X. Liu, Y. Yao, L. Dong, B. Li, MOF-74-M (M = Mn, Co, Ni, Zn, MnCo, MnNi, and MnZn) for low-temperature NH3-SCR and in situ DRIFTS study reaction mechanism, *ACS Appl. Mater. Interfaces* 12 (2020) 48476–48485. <https://doi.org/10.1021/acsami.0c11035>.

[34] H. Liu, Z. Fan, C. Sun, S. Yu, S. Feng, W. Chen, D. Chen, C. Tang, F. Gao, L. Dong, Improved activity and significant SO2 tolerance of samarium modified $\text{CeO}_2\text{-TiO}_2$ catalyst for NO selective catalytic reduction with NH3, *Appl. Catal. B* 244 (2019) 671–683. <https://doi.org/10.1016/j.apcatb.2018.12.001>.

[35] J. Yang, S. Ren, Y. Zhou, Z. Su, L. Yao, J. Cao, L. Jiang, G. Hu, M. Kong, J. Yang, Q. Liu, In situ IR comparative study on N2O formation pathways over different valence states manganese oxides catalysts during NH3-SCR of NO, *Chem. Eng. J.* 397 (2020) 125446. <https://doi.org/10.1016/j.cej.2020.125446>.

[36] A. Marberger, D. Ferri, M. Elsener, O. Krocher, The significance of lewis acid sites for the selective catalytic reduction of nitric oxide on vanadium-based catalysts, *Angew. Chem. Int. Ed.* 55 (2016) 11989–11994. <https://doi.org/10.1002/anie.201605397>.

[37] M. Zhu, J.-K. Lai, U. Tumuluri, Z. Wu, I.E. Wachs, Nature of active sites and surface intermediates during SCR of NO with NH3 by supported V2O5-WO3/TiO2 catalysts, *J. Am. Chem. Soc.* 139 (2017) 15624–15627. <https://doi.org/10.1021/jacs.7b09646>.

[38] V. Thanh Huyen, J. Radnik, J. Rabeha, U. Bentrup, M. Schneider, H. Atia, U. Armbruster, W. Gruenert, A. Brueckner, Efficient VOx/Ce1-xTiO2 catalysts for low-temperature NH3-SCR: reaction mechanism and active sites assessed by in situ/operando spectroscopy, *ACS Catal.* 7 (2017) 1693–1705. <https://doi.org/10.1021/acs.catal.6b03223>.

[39] H. Wang, H. Chen, Y. Wang, Y.-K. Lyu, Performance and mechanism comparison of manganese oxides at different valence states for catalytic oxidation of NO, *Chem. Eng. J.* 361 (2019) 1161–1172. <https://doi.org/10.1016/j.cej.2018.12.159>.

[40] L.J. France, W. Li, Y. Zhang, W. Mu, Z. Chen, J. Shi, Q. Zeng, X. Li, A superior Fe-Zr mixed oxide catalyst for the simultaneous reduction of NO and SO2 with CO, *Appl. Catal. B* 269 (2020) 118822. <https://doi.org/10.1016/j.apcatb.2020.118822>.

[41] X. Cheng, X. Zhang, D. Su, Z. Wang, J. Chang, C. Ma, NO reduction by CO over copper catalyst supported on mixed CeO_2 and Fe_2O_3 : catalyst design and activity test, *Appl. Catal. B* 239 (2018) 485–501. <https://doi.org/10.1016/j.apcatb.2018.08.054>.

[42] X. Zhang, X. Zhang, X. Yang, Y. Chen, X. Hu, X. Wu, CeMn/TiO_2 catalysts prepared by different methods for enhanced low-temperature NH3-SCR catalytic performance, *Chem. Eng. Sci.* 238 (2021). <https://doi.org/10.1016/j.ces.2021.116588>.

[43] G. Li, D. Mao, M. Chao, G. Li, J. Yu, X. Guo, Low-temperature NH3-SCR of NO over $\text{MnCeO}_2\text{/TiO}_2$ catalyst: Enhanced activity and SO2 tolerance by modifying TiO_2 with Al_2O_3 , *J. Rare. Earth.* 39 (2021) 805–816. <https://doi.org/10.1016/j.jre.2020.10.001>.

[44] F. Liu, W. Shan, Z. Lian, J. Liu, H. He, The smart surface modification of Fe_2O_3 by WO_x for significantly promoting the selective catalytic reduction of NOx with NH3, *Appl. Catal. B* 230 (2018) 165–176. <https://doi.org/10.1016/j.apcatb.2018.02.052>.

[45] P. Wang, S. Chen, S. Gao, J. Zhang, H. Wang, Z. Wu, Niobium oxide confined by ceria nanotubes as a novel SCR catalyst with excellent resistance to potassium, phosphorus, and lead, *Appl. Catal. B* 231 (2018) 299–309. <https://doi.org/10.1016/j.apcatb.2018.03.024>.

[46] J. Liu, Y. Wei, P.-Z. Li, P. Zhang, W. Su, Y. Sun, R. Zou, Y. Zhao, Experimental and theoretical investigation of mesoporous MnO_2 nanosheets with oxygen vacancies for high-efficiency catalytic DeNOx, *ACS Catal.* 8 (2018) 3865–3874. <https://doi.org/10.1021/acscat.8b00267>.

[47] H. Hu, S. Cai, H. Li, L. Huang, L. Shi, D. Zhang, Mechanistic aspects of deNOx processing over TiO_2 supported Co-Mn oxide catalysts: structure-activity relationships and in situ DRIFTS analysis, *ACS Catal.* 5 (2015) 6069–6077. <https://doi.org/10.1021/acscat.5b01039>.

[48] W.S. Kijlstra, D.S. Brands, H.I. Smit, E.K. Poels, A. Bliek, Mechanism of the selective catalytic reduction of NO by NH3 over $\text{MnO}_x\text{/Al}_2\text{O}_3$, *J. Catal.* 171 (1997) 219–230. <https://doi.org/10.1006/jcat.1997.1789>.

[49] X. Zhang, D. Wang, F. Cheng, M. Lu, B. Xiong, Influence of Mn doping on magnetic $\gamma\text{-Fe}_2\text{O}_3$ catalysts for selective catalytic reduction at low temperatures, *J. Eng. Thermophys.* 35 (2014) 995–998.

[50] S. Dong, H. Wang, T. Zhu, Z. Qu, High-performance Fe-Cu composite oxide for selective catalytic reduction of NOx with NH3: driving of Cu on $\alpha\text{-Fe}_2\text{O}_3$, *J. Environ. Chem. Eng.* 10 (2022) 108481. <https://doi.org/10.1016/j.je.2022.108481>.

[51] C. Liu, Y. Bi, J. Li, Activity enhancement of sulphated Fe_2O_3 supported on $\text{TiO}_2\text{-ZrO}_2$ for the selective catalytic reduction of NO by NH3, *Appl. Surf. Sci.* 528 (2020) 146695. <https://doi.org/10.1016/j.apsusc.2020.146695>.

[52] Y. Fan, J. Zhang, L. Yang, M. Lu, T. Ying, B. Deng, W. Dai, X. Luo, J. Zou, S. Luo, Enhancing SO2-shielding effect and Lewis acid sites for high efficiency in low-temperature SCR of NO with NH3: Reinforced electron-deficient extent of Fe^{3+} enabled by Ti^{4+} in Fe_2O_3 , *Sep. Purif. Technol.* 311 (2023) 123272. <https://doi.org/10.1016/j.seppur.2023.123272>.

[53] L. Zhu, J. Yao, G. Ma, P. Cao, S. Wu, Z. Li, NH3-SCR performance and SO2 resistance comparison of CeO_2 based catalysts with Fe/Mo additive surface decoration, *Chem. Eng. J.* 428 (2022) 131372. <https://doi.org/10.1016/j.cej.2021.131372>.

[54] L. Han, M. Gao, J.-y. Hasegawa, S. Li, Y. Shen, H. Li, L. Shi, D. Zhang, SO2-Tolerant Selective Catalytic Reduction of NOx over Meso- $\text{TiO}_2\text{/Fe}_2\text{O}_3\text{/Al}_2\text{O}_3$ Metal-Based Monolith Catalysts, *Environ. Sci. Technol.* 53 (2019) 6462–6473. <https://doi.org/10.1021/acs.est.9b00435>.

[55] X. Huang, N. Fang, S. Wu, F. Dong, Y. Chu, Z. Tang, Interfacial confinement effect induced by pre-sulfurization for promoting SO2 tolerance of MnFe-TOS catalyst in low-temperature NH3-SCR reaction, *Appl. Catal. B* 343 (2024) 123518. <https://doi.org/10.1016/j.apcatb.2023.123518>.

[56] Z. Chen, Q. Liu, L. Guo, S. Zhang, L. Pang, Y. Guo, T. Li, The promoting mechanism of in situ Zr doping on the hydrothermal stability of Fe-SSZ-13 catalyst for NH3-SCR reaction, *Appl. Catal. B* 286 (2021) 119816. <https://doi.org/10.1016/j.apcatb.2020.119816>.

[57] Y. Zeng, W. Song, Y. Wang, S. Zhang, T. Wang, Q. Zhong, Novel Fe-doped CePO_4 catalyst for selective catalytic reduction of NO with NH3: the role of Fe^{3+} ions, *J. Hazard. Mater.* 383 (2020) 121212. <https://doi.org/10.1016/j.jhazmat.2019.121212>.

[58] Y. Hou, J. Wang, Q. Li, Y. Liu, Y. Bai, Z. Zeng, Z. Huang, Environmental-friendly production of FeNbTi catalyst with significant enhancement in SCR activity and SO2 resistance for NOx removal, *Fuel* 285 (2021) 119133. <https://doi.org/10.1016/j.fuel.2020.119133>.

[59] K. Zha, C. Feng, L. Han, H. Li, T. Yan, S. Kuboon, L. Shi, D. Zhang, Promotional effects of Fe on manganese oxide octahedral molecular sieves for alkali-resistant catalytic reduction of NOx: XAFS and in situ DRIFTS study, *Chem. Eng. J.* 381 (2020) 122764. <https://doi.org/10.1016/j.cej.2019.122764>.

[60] H. Wang, P. Ning, Y. Zhang, Y. Ma, J. Wang, L. Wang, Q. Zhang, Highly efficient $\text{WO}_3\text{-Fe}_2\text{O}_3$ catalysts synthesized using a novel solvent-free method for NH3-SCR, *J. Hazard. Mater.* 388 (2020) 121812. <https://doi.org/10.1016/j.jhazmat.2019.121812>.